CHAPTER 2

Numerical and Experimental Study of Internal Flow Field

for a Carbon Fiber Tow Pneumatic Spreader
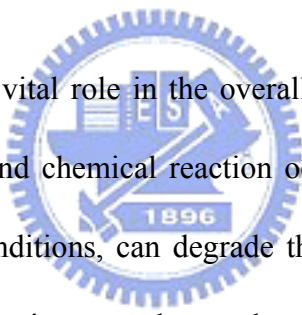
Numerical and Experimental Study of Internal Flow Field for a Carbon Fiber Tow Pneumatic Spreader

Abstract

In this study, a three-dimensional mathematical model of a fiber pneumatic spreader was successfully developed in the physical phenomena of the internal flow field by a far field treatment at boundary conditions. The three-dimensional numerical analysis was carried out on incompressible fluid flows in the pneumatic spreader by using finite volume method combined with the k- turbulence model which solves Reynolds-averaged Naiver-Stokes equations. Characteristics of the flow field in the spreader at different service conditions are investigated by velocity and pressure distributions. Comparisons of numerical results with measured velocity and pressure distributions were made to determine the accuracy of the employed method. A good agreement was found in both qualitative and quantitative analysis. Fibers were spread on 1:1-scale model of the pneumatic spreader at various fiber transporting rates and air flow rates. Photography techniques were simultaneously used to record the procedures of fibers spread. The carbon fiber tow was easily spread out at service conditions. The performance was better than prior studies in one-dimensional orifice formulation. The results revealed details of the fiber spreading processes. Agreement among those results validated the assumptions inherent to the computational calculation and gave confidence to more complex geometries as well as flow fields. In other words, the use of numerical analysis in the internal flow field was useful for the fiber pneumatic spreader design.

. Introduction

Over the years, carbon fibers have been considered as one of the most important reinforcements for aluminum and its alloy to fabricate advanced composite materials. The carbon fiber (CF) reinforcement/aluminum (Al) matrix composites are of great interest because of their high specific strength and stiffness, low coefficient of thermal expansion and high thermal/electric conductivity. Therefore, CF/Al composites have the most potential application as structural and functional materials in future. The primary concern in achieving the potential has been the difficulties experienced in combining Al with continuous fiber tows and the chemical reaction at interface between CF and Al.

The interface plays a most vital role in the overall performance of the composite materials. Improper wetting and chemical reaction occurring at the interface during synthesis or under service conditions, can degrade the mechanical properties of the composites [1-11]. The reaction at the carbon-aluminum interface at high temperatures to form aluminum carbide has long been considered to affect critically the strength of C/Al composites [12, 13]. The formation of aluminum carbide at the fiber-matrix interface was considered to induce poor composite properties, as observed by Pepper and Pent [14], Xiangun and Hanlin[15]. However, the tensile strength of the composite improved considerably after small amounts of carbide were generated. The apparent inconsistency between the results is attributable, to some extent, to the presence of various fibers and/or processing methods. Further work is clearly required to help resolve the issue.

Recent advances in the synthesis of carbon nanotubes have enabled the growth of

carbon nanotubes on carbon fibers using chemical vapor deposition (CVD) [16]. Carbon nanotubes were synthesized on the surface of carbon fibers and the fiber/matrix interfacial properties were assessed, and the results found that the presence of carbon nanotubes at the fiber/matrix interface improves the interfacial shear strength of the composites. With carbon nanotubes, the change in reinforcement scale relative to carbon fibers offers opportunity to combine potential benefits of nanoscale reinforcement with well-established fibrous composites to create multiscale hybrid micro/nanocomposites. By varying the reinforcement scale, it may be possible to tailor the mechanical and physical properties of the composites. Unfortunately, during catalyst application, the catalyst layer may not always be deposited uniformly on the surface of the individual fiber. As a consequence, there will be local areas on the fiber where amorphous carbon is deposited instead of nanotubes as synthesis of carbon nanotubes on carbon fibers.

The mechanical properties of composites depend on not only the properties of the constituent materials but also the nature of the interfacial bond and the mechanism of load transfer, the topic of the fiber/matrix interface, or "interphase" has been the subject of considerable research. For carbon fibers, a number of surface treatments have been used to improve adhesion at the fiber/matrix interface. Certain coatings can promote the wettability between CF filaments and Al as well as prevent the molten aluminum coming into direct contact with carbon; thus the chemical reaction can be eliminated. Also, interfacial adhesion is typically improved by enhancing the chemical interaction at the interface or by increasing the fiber surface area, providing a larger area over which to transfer load. Many methods have been proposed for the preparation of metallic or non-metallic coated carbon fiber tow [9,17-20]. However,

the observed variation in the coating is mainly owing to non-uniform activation on the surface of the fibers prior to deposition. The non-uniform activation is caused by the contact of carbon fiber. Bobka et al. [17, 21, 22] reported that oxidation treatment led to a non-uniform etching of the fibers when carbon fiber tows were treated by oxygen to modify the surface of the filaments. Therefore, the outer filaments are strongly attacked while those in the interior of the bundle are hardly attacked.

Some variations in the coating techniques of carbon fiber tows have been developed. Ceramic coatings (SiC, TiC, TiB_2) or functionally gradient coatings (C/SiC/Si) were deposited by chemical vapor deposition (CVD) on carbon filaments for CF/Al composites; however, the similar results were found that fibers and composites decrease in strength with coating thickness and the variations of coating thickness in carbon fiber tow are obvious[2,7,9]. The main problem still exists, which comes from the different treatment between the outer and the interior filaments due to the carbon fiber tows containing thousands of filaments, in spite of the deposition technologies and the deposited materials developed. Therefore, if the carbon fibers are separated uniformly, it is advantageous for the improvement of mechanical properties [23].

Processes and apparatus were developed for pneumatically spreading graphite or other carbon filaments from a tow bundle to form a sheet or a ribbon in which the filaments were maintained in parallel [24-29]. The developmental history of the pneumatic spreading system was briefly introduced in previous chapter. The key component in the pneumatic spreading system is the spreader as shown in Fig. 2-1. The carbon fiber tow is comprised of thousands of filaments and the carbon filaments are interacted with air in the spreader.

Baucom and Marchello [30] were the first to tackle the design of pneumatic

spreader; they modeled a single fiber suspended in air under both a pressure drop and tow tension, and derived a formulation from orifice equation to predict the fiber tow spread angle in the spreader. It is suggested that the tow spread may be correlated as a function of fiber tension and pressure drop. Comparisons of the experimental data for a 12k tow (containing 12,000 filaments) with the single fiber prediction showed that the results were not satisfactory because the flow-field was too complicated.

None of the previous works investigated the internal flow patterns in qualitative and quantitative analysis about the spreader. Therefore, the exact flow-field of the spreader is still unknown. The computational fluid dynamics (CFD) methodology is a traditional numerical method for viscous fluid flow simulation. It has been successfully implemented in CVD process simulation, turbo-machinery design, heat transfer analysis, and many other fluid flow-related problems. Major contributions of this approach include providing detailed flow field of the fluid while flowing through the pipes, machines, channels, etc., with enough accuracy for engineering designs; fast response to design changes such that long-term trial-and-error process can be eliminated; and saving cost for prototype development since the performances of the design can be simulated and displayed on a computer display before actual system are manufactured. Hence, the objective of the present study is to establish three-dimensional (3-D) mathematical model of the spreader by using a numerical technique of far field treatment and to provide a 3-D numerical flow visualization which reveals velocity fields, pressure distributions, streamlines and useful flow patterns. The flow patterns contribute to understanding the detail flow-field in the physical model, and then help us to develop a new efficient spreader. Finally, a pneumatic spreading system is constructed. In this model system, carbon fiber sheet can be prepared from fiber tow. Meanwhile, photography is used to record

the carbon fiber tow spreading process. The spreading mechanism of the carbon filaments is also investigated by combing numerical simulation and experimental analysis.

. Governing Equations and Turbulence Model

2.1 Governing equations

The basic set of equations solved by **Navier-Stokes** equation program for laminar flows comprises equations for conservation of mass and momentum and, in a non-isothermal flow, energy. These are the continuity equation [31].

$$\frac{\partial \rho}{\partial t} + \nabla \cdot (\rho U) = 0, \qquad (2.1.1)$$

the momentum equation

$$\frac{\partial \rho U}{\partial t} + \nabla \cdot (\rho U \otimes U) = B + \nabla \cdot \sigma, \qquad (2.1.2)$$

where   is the stress tensor:

$$\sigma = -p\delta + (\zeta - \frac{2}{3}\mu)\nabla \cdot U\delta + \mu(\nabla U + (\nabla U)^T), \qquad (2.1.3)$$

and the energy equation:

$$\frac{\partial \rho H}{\partial t} + \nabla \cdot (\rho UH) - \nabla \cdot (\lambda \nabla T) = \frac{\partial p}{\partial t}, \qquad (2.1.4)$$

where *H* is the total enthalpy, given in terms of the static (thermodynamic) enthalpy h by:

$$H = h + \frac{1}{2}U^2. \qquad (2.1.5)$$

Here   is the fluid density, U=(*U,V,W*) the fluid velocity, *p* the pressure, *T* the temperature and *t* is time. Further *B* is a body force, μ is the molecular viscosity,   is the bulk viscosity and   is the thermal conductivity. If the flow is incompressible, the fluid density is constant,   = $_0$.

2.2 Turbulence Models

Turbulent flows are extremely complex time-dependent flows. They are governed by the laminar flow equations discussed in §2.1. However, it is not feasible to solve these to the required accuracy using current technology, except for low Reynolds numbers in simple geometries. We therefore resort to turbulence models, which solve transport equations for the Reynolds-averaged quantities [32, 33]:

$$\overline{\Phi}(t) = \frac{1}{2\delta t} \int_{t-\delta t}^{t+\delta t} \Phi(\tau) d\tau \qquad (2.2.1)$$

where δt is a time scale large relative to the time scale of turbulent fluctuations, and small relative to the time scale to which we wish to resolve. Splitting fields into their mean and fluctuating parts:

$$\Phi = \overline{\Phi} + \phi, \qquad\qquad \Psi = \overline{\Psi} + \psi$$
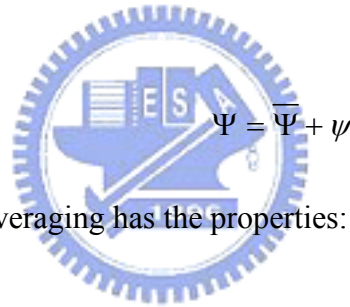
We easily see that Reynolds averaging has the properties:

1. $\overline{\overline{\Phi}} = \overline{\Phi}, \qquad \overline{\phi} = 0.$

2. $\overline{a\Phi + b\Psi} = a\overline{\Phi} + b\overline{\Psi}, \qquad a, b \quad cons \tan t.$

3. $\overline{\Phi\Psi} = \overline{\Phi}\overline{\Psi} + \overline{\phi\psi}$

4. $\dfrac{\overline{\partial\Phi}}{\partial t} = \dfrac{\partial\overline{\Phi}}{\partial t}, \qquad \dfrac{\overline{\partial\Phi}}{\partial x^i} = \dfrac{\partial\overline{\Phi}}{\partial x^i}.$

From now on, we drop the bars from Reynolds averaged mean quantities for all primitive variables; we retain the bars however for averages involving products of fluctuating quantities. The derivations of the following results assume that the flow is incompressible.

Applying Reynolds averaging to the continuity equation (2.1.1), the momentum

equation (2.1.2), and the scalar transport equation, we obtain:

$$\frac{\partial \rho}{\partial t} + \nabla \cdot (\rho U) = 0, \tag{2.2.2}$$

$$\frac{\partial \rho U}{\partial t} + \nabla \cdot (\rho U \otimes U) = B + \nabla \cdot (\sigma - \rho \overline{u \otimes u}), \tag{2.2.3}$$

$$\frac{\partial \rho \Phi}{\partial t} + \nabla \cdot (\rho U \Phi) = \nabla \cdot (\Gamma \nabla \Phi - \rho \overline{u \phi}) + S. \tag{2.2.4}$$

Hence, the Reynolds-averaged continuity equation is the same as the equation that has not been averaged. However, the momentum and scalar transport equations contain turbulent flux terms additional to the molecular diffusive fluxes. These are the

$$\text{Reynolds stress} = \rho \overline{u \otimes u}, \tag{2.2.5}$$

and the

$$\text{Reynolds flux} = \rho \overline{u \phi}. \tag{2.2.6}$$

In incompressible and weakly compressible flow, the contributions from the mean and turbulent kinetic energies are ignored. Turbulence models close equations (2.2.1)~ (2.2.6) .by providing models for the computation of the Reynolds stresses and Reynolds fluxes. The models that we use can be put into two broad classes, eddy viscosity models and second order closure models.

These models the Reynolds stresses and fluxes algebraically in terms of known mean quantities. To be precise, we have the eddy viscosity hypothesis that the Reynolds stresses can be linearly related to the mean velocity gradients in a manner analogous to the relationship between the stress and strain tensors in laminar Newtonian flow:

$$-\rho \overline{u \otimes u} = -\frac{2}{3} \rho \kappa \delta - \frac{2}{3} u_T \nabla \cdot U \delta + u_T (\nabla U + (\nabla U)^T) \tag{2.2.7}$$

Here, $\kappa = \frac{1}{2}\overline{u^2}$. is the turbulent kinetic energy, and μ_T is an additional viscosity, called the eddy viscosity or the turbulent viscosity.

2.3 $\kappa - \varepsilon$ Models

The $\kappa - \varepsilon$ model uses an eddy-viscosity hypothesis for the turbulence. The continuity and momentum equations are then:

$$\frac{\partial \rho}{\partial t} + \nabla \cdot (\rho U) = 0, \tag{2.3.1}$$

and

$$\frac{\partial \rho U}{\partial t} + \nabla \cdot (\rho U \otimes U) - \nabla(\mu_{eff} \nabla U) = -\nabla P' + \nabla(\mu_{eff}(\nabla U)^T) + B. \tag{2.3.2}$$

and U are now the mean fluid density and velocity, μ_{eff} is the effective viscosity defined by:

$$\mu_{eff} = \mu + \mu_T$$

where μ_T is the turbulent viscosity and *B* is the body force.

In the $\kappa - \varepsilon$ model, it is assumed that

$$\mu_T = C_\mu \rho \frac{\kappa^2}{\varepsilon}. \tag{2.3.3}$$

The transport equations for the turbulence kinetic energy and turbulence dissipation rate are

$$\frac{\partial \rho \kappa}{\partial t} + \nabla \cdot (\rho U \kappa) - \nabla(\mu + \frac{\mu_T}{\sigma_\kappa} \nabla \kappa) = P + G - \rho \varepsilon \tag{2.3.4}$$

and

$$\frac{\partial \rho \varepsilon}{\partial t} + \nabla \cdot (\rho U \varepsilon) - \nabla(\mu + \frac{\mu_T}{\sigma_\varepsilon} \nabla \varepsilon) = C_1 \frac{\varepsilon}{\kappa}(P + C_3 \max(G,0)) - C_2 \rho \frac{\varepsilon^2}{\kappa} \tag{2.3.5}$$

respectively, where *P* is the shear production defined by:

$$P = \mu_{eff} \nabla U . (\nabla U + \nabla U)^T) - \frac{2}{3} \nabla \cdot U (\mu_{eff} \nabla \cdot U + \rho \kappa) \qquad (2.3.6)$$

and G is production due to the body force defined by:

$$G = G_{buoy} + G_{res}, \qquad (2.3.7)$$

were G_{buoy}, G_{rot} and G_{res} are terms representing production due to buoyancy, rotation and resistances respectively. However $G_{rot} = 0$, and only G_{buoy} is included in the code. Therefore $G = G_{buoy}$ and is defined by:

$$G = -\frac{\mu_{eff}}{\rho \sigma_\rho} g \cdot \nabla \rho, \qquad (2.3.8)$$

$$G = \frac{1}{2} trace(G)$$
$$= \begin{cases} - \rho \beta g \cdot \overline{uh} + \rho \alpha g \cdot \overline{us} & \text{if incompressible flow,} \\ - a_h \rho \overline{uh} \cdot \nabla p - a_s \rho \overline{us} \cdot \nabla p & \text{if compressible flow.} \end{cases} \qquad (2.3.9)$$

2.4 Reynolds-averaged Navier-Stokes and $\kappa - \varepsilon$ Models

Therefore, the incompressible and isothermal Reynolds-averaged Navier-Stokes equations are:

$$\frac{\partial u_j}{\partial x_j} = 0$$

$$\frac{\partial u_i}{\partial t} + \frac{\partial u_i u_j}{\partial x_i} + \frac{1}{\rho} \frac{\partial p}{\partial x_j} + \frac{\partial}{\partial x_j} \left(\overline{u'_i u'_j} \right)$$
$$- \frac{\partial}{\partial x_j} \left[\nu \left(\frac{\partial u_i}{\partial x_j} + \frac{\partial u_j}{\partial x_i} \right) \right] = 0 \quad , \quad i, j = 1, 2, 3$$

where u_j is the velocity; p is the pressure; ρ is the constant density, and ν is the molecular kinematic viscosity. The u_i', u_j' are the fluctuation parts of the velocity u_i and u_j ; $\overline{u_i'u_j'}$ is the Reynolds stress tensor which can be modeled by the eddy viscosity hypothesis:

$$\overline{u_i'u_j'} = \tilde{\tau}_{ij} = \frac{1}{\rho}\hat{\tau}_{ij} = \frac{2}{3}\delta_{ij}k - \frac{2}{3}\nu_T\nabla\cdot u_i\delta_{ij} + \nu_T\left(\nabla u_i + \left(\nabla u_i\right)^T\right)$$

Here, k= $\frac{1}{2}\overline{u}^2$ is the turbulent kinetic energy, and ν_T is the eddy viscosity. They have to be prescribed by a turbulent model.

The generic k-ε model can be described as [24]:

$$\rho\frac{\partial k}{\partial t} + \rho\nabla\cdot\left(u_i k\right) = \nabla\cdot\left(\left(\nu + \sigma_k\nu_T\right)\nabla k\right) + \tilde{\tau}_{ij}\nabla\cdot u_i - \rho\varepsilon$$

$$\rho\frac{\partial\varepsilon}{\partial t} + \nabla\cdot\left(u_i\varepsilon\right) = \nabla\cdot\left(\left(\nu + \sigma_\varepsilon\nu_T\right)\nabla\varepsilon\right) + c_1\varepsilon/k\,\tilde{\tau}_{ij}\nabla\cdot u_i - c_2\rho\frac{\varepsilon^2}{k}$$

where $\qquad\sigma_k = \dfrac{k^2}{\left(c_2 - c_1\right)\sqrt{c_\mu}}$

k (Von Karman constant) = 0.4187

The eddy viscosity is calculated from:

$$\nu_T = c_\mu\rho\frac{k^2}{\varepsilon}$$

Where σ_k and σ_ε are the turbulent Prandtl number for k and ε, respectively, and the c_1, c_2 and c_μ are the empirical coefficient [31]. The set of model constants employed is summarized in Table .

. Boundary Fitted Coordinate and Grid Generation

In fact, the geometry of a spreader is too complex to be described by using natural analytic coordinates such as cylindrical coordinates, spherical coordinates or bipolar coordinates. In this case, the coordinate transformation must be given numerically. There is now extensive literature on the numerical generation of boundary fitted grids [30, 31]. Boundary fitted coordinates extend the capabilities of finite difference methods to deal with complex geometry. The basic idea is to use a curvilinear coordinate transformation, mapping the complex flow domain in physical space to a simple flow domain in computational space. In other words, the Cartesian coordinate system $\left(x^{i} \right) = \left(x, y, z \right)$ in the physical domain is replaced by a curvilinear coordinate system $\left(\xi^{i} \right) = \left(\xi, \eta, \zeta \right)$ such that boundaries of the flow domain correspond to surface.

The equations are discretised with respect to the computational space coordinate. The grid must be generated for the region of interest to allow the routine computational solution of the equation, and the boundary conditions may be implemented naturally in the rectangular computational domain. When solving three-dimensional nonlinear systems of partial differential equations in domains with complex geometry, the generation of the gird may be the most time-consuming part of the calculation. In fact, it may take more man-hours to generate a grid than it does to represent and analyze the solution on the grid. The expense of making the partial differential equations would be higher due to the non-linear coordination transformation, and great deal of memory is wasted because of the necessity of designating a large proportion of the grid as solid. The multi-block approach was used

in order to maximize computational efficiency and save memory [31, 34].

The main reasons for using multiblock grids rather than single-block grids are that

(1) the geometry of the region is complicated, having a multiply connected boundary, cuts, narrow protuberances, cavities, etc.;

(2) the physical problem is heterogeneous relative to some of the physical quantities, so that different mathematical models are required in different zones of the domain to adequately describe the physical phenomena;

(3) the solution of the problem behaves non-uniformly: zones of smooth and rapid variation of different scales may exist.

The concept of the multi-block grid is the solution domain, which is divided into subdomains. Each subdomain has its associated subgrid, or block. In multi-block grids, data is transferred from one block to another using a generalization of the periodic boundary condition. The blocks are arranged to overlap such that a boundary surface of one block is situated in the interior of another. After each iteration, the value of variables on the boundary of the first block must cross a boundary surface of the second block; values of variables on this boundary surface can be updated using interior values from the first block.

As shown in Fig 2-2(a), the geometry of the 3-D spreader model was defined first in a physical space (x, y, z). Since it was symmetrical in the vertical plane (x-y plane), to reduce computer time only half of the geometry was simulated. In most work of simulation, the boundary conditions at inlets used were a uniform velocity that was quoted from measured data, or used ambient pressure for an internal flow

field. In the present study, the inlet velocity was unknown. It was difficult to measure for a sudden contraction case. Therefore, we considered the realistic status as the characterization of the fluid flow in the far field. Thus, the computation domain was extended along x-direction and y-direction as Fig. 2-2(b) and (c) illustrate (a perspective view and an enlarged view, respectively).

The blocks were built on each side of the spreader model. Therefore, the boundary conditions at the outer surface of each block could be specified by atmospheric pressure (101300 Pa), and the computation of the flow field was executed from external flow field to internal flow field. The grid employed was structured and orthogonal curvilinear. The number of nodes and elements were 137,800 and 129,600 in the fluid domain respectively. A grid convergence study was performed to ensure that the resolution of this mesh was adequate. Doubling the number of nodes changed the solution by less than 0.01 pct.
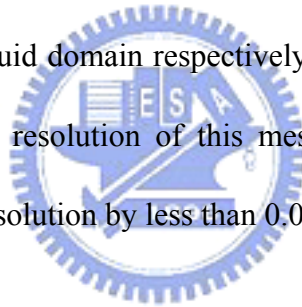
. Computational Details

A. Boundary Conditions

Quite a few published papers discuss and stress the importance of specification of the inlet boundary conditions in the computation of turbulent flows. Sturgess et al. [35] showed that the numerical simulations of flows were highly sensitive to the assumptions made for inlet boundary conditions. Choice of the computational grid was also important. They concluded that overall accuracy of the simulation is determined by assumed boundary conditions and choice of grid. Eaton and Johnston [36] cited that a backward-facing step flow is affected by inlet boundary conditions. They suggested that accurate specification for the inlet boundary conditions including mean velocity and turbulence details is essential to correctly describe the downstream flow field. The boundary conditions employed were as follows.

(1) Symmetry plane:

$$V = W = 0$$

$$\frac{\partial U}{\partial x} = 0 \quad , \quad \frac{\partial \phi}{\partial x} = 0$$

where $\phi = k , \varepsilon \text{ and } p$

(2) Pressure boundaries:

In the mathematical grid, the computational domains were extended so that the pressure boundaries could be easily created and specified on the surfaces of the blocks as the inlet boundary conditions, as shown in Fig. 2-2(b). For the surfaces were sufficiently far downstream, fixed values of all variables could be specified at pressure boundaries.

$$p = 101300 \text{ (Pa)} \qquad \text{(atmospheric condition)}.$$

$$U = V = W = 0 \qquad \text{(free stream)}$$

(3) Outlet

Static pressure was introduced at the outlet location to model the outflow boundary. For observing the flow field in the 3-D spreader model, various static pressure conditions were used for computation, which were 101100 Pa, 101200 Pa and 101250 Pa respectively. It was useful to predict the experimental condition and make a comparison of velocities computed by various pressure and measured data.

(4) Walls

The boundary wall was fixed, and a no-slip condition was imposed on all velocity components. Many of variables varied rapidly in the near wall regions of the flow, instead of using extremely fine grids in these regions; therefore, their behavior was specified with wall functions. The wall functions were illustrated below by considering the flow in a fully-developed boundary layer over a stationary wall [33]. Near the wall (y=d), it was found that the wall shear stress τ is related to the turbulence kinetic energy by

$$\tau^2 = c_\mu \rho^2 k^2$$

A new quantity is defined such that

$$\tau_k = \rho \, c_\mu^{\frac{1}{2}} \, k$$

This may be used to define scaled variables

$$u^+ = -\frac{\left(\rho \tau_k\right)^{\frac{1}{2}}}{\tau} u$$

and

$$y^+ = -\frac{\left(\rho \tau_k\right)^{\frac{1}{2}}}{\mu}\left(d - y\right)$$

34

The scaled velocity component parallel to the wall and in the x directions is
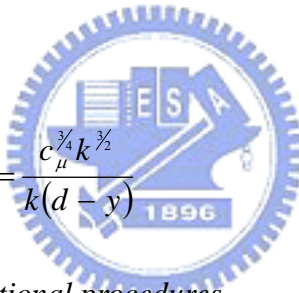
$$u^+ = \begin{cases} y^+, \text{ for } y^+ < y_0^+ \\ \dfrac{1}{k}\log(Ey^+), \text{ for } y^+ > y_0^+ \end{cases}$$

where log is a natural logarithm.

The cross-over point y_0^+ between the viscous sub-layer and the logarithmic region is the upper root of

$$y_0^+ = \frac{1}{k}\log(Ey_0^+)$$

The equation for the turbulence kinetic energy k is solved in the control volume immediately adjacent to the wall. From the value of the wall shear stress τ can be obtained. The turbulence dissipation is obtained from the turbulence kinetic energy through the relation

$$\varepsilon = \frac{c_\mu^{3/4} k^{3/2}}{k(d-y)}$$

B. *Discretization and computational procedures*

Discretization has been carried out using the finite volume method. The governing equations were integrated over the control volume and reduced to algebraic equations which followed conservation laws. Once a grid of points was set up over the field, where all the unknown variables were stored in the certain of the computational cells. In order to avoid pressure-velocity decoupling problems, arising from the fact that pressure and velocity were calculated in the same location, the convection flux through each cell face was calculated by using the modification first `proposed by Rhie and Chow [37], extended here for a multi-block grid. The major achievement of this approach is that it provides a prescription for implementing the

standard primitive variable algorithms such as SIMPLE and SIMPLEC using a non-staggered grid. The feature of the prescription is that the velocity needed for the calculation of the connective flux through a cell face is not obtained from a linear interpolation of the adjacent cells' velocities. However the velocity is modified to be directly linked to the two adjacent pressure nodes. Following this procedure, SIMPLE algorithm was used as a pressure-correction method [38, 39], in order to derive the pressure equation from the continuity equation.

The treatment of the convection term determines the accuracy of the solutions of the model equations. The CCCT scheme was used for the discretization of convective fluxes. The CCCT scheme is a modification of the quadratic upwind differencing scheme (QUICK) which is an upwind scheme with third-order accuracy, and can suffer from non-physical overshoots in its solutions [37]. The diffusion terms were discretized in space using second-order centered difference scheme. The set of linearised difference equations, after the discretization of the conservation equations, were passed to a simultaneous linear equation solver which used an iterative solution method. STONE method was available for this purpose and was very efficient in a vector computer. In this work, since the transient evolution was not of interest, the time stepping scheme could be optimized for faster convergence. Acceleration techniques like false time step were applied [31].

Therefore, a typical simulation of 3-D model on the base mesh required 300 MB of memory, and consumed total CPU time 7.237×10^4 second. The program was executed on a vector computer, CRAYJ916 super computer, with eight 100MHz processors and 1GB main system RAM.

Ⅱ. Experiment

A. *Experimental Setup*

Experiments were conducted using the setup shown schematically in Fig. 2-1. The main elements were comprised in sequence of: the tow feed spool, tension control device, the pneumatic tow spreader, vacuum pump and take-up spool. The fibers from the carbon fiber tow containing 12,000 filaments were passed through a fiber guide into a first friction roller. The first roller was synchronized with second friction roller at a constant rate of speed. The two rollers were controlled by a variable speed driver. Hence, the fibers between the two rollers, which were subsequently spread in the pneumatic spreader, remained in a low tensional state that was given by tension control device. For the air flow rate in the pneumatic spreader, the vacuum pump sucked air, and gave a stable control of flow rate which was measured by a multiple tube flow meter and precision pressure controller. After the fibers spread and left the second roller, the fibers were taken up by a take-up system.

B. *Experimental Techniques.*

The design of the spreader must satisfy several interacting requirements. Although high air velocity resulting drag force to fibers is desirable, streamwise velocity is constrained by the need to avoid circulation and excessive agitation of the airflow. Agitation can cause fibers to entangle, which make fiber spreading difficult and damages fibers. This is the first three-dimensional mathematical model of a pneumatic spreader. Therefore, the height of the spreader and the distance from the symmetry plane to the clapboard were the two designed parameters in the spreader.

The spreader formed by PAN (polyacrylonitrile) pieces, which were transparent allowing the spread procedure of carbon fibers to be photographed for subsequent qualitative comparison with computational results, had a through-length 500mm in the x-direction as shown in Fig. 2-2(a). The half width of the spreader was one fourth (125mm) of the length.

The projecting part connected to vacuum pump had the width 80mm in the z direction and length 110mm in the x direction. The fiber entrance named inlet-2 was 2.5mm in half width. The fiber exit named inlet-1 has 25mm in half width selected as the final fiber spread width. The clapboard contained nine slots were parallel to the symmetry plane.

Each slot was 5mm wide and 10mm apart; the first slot was behind the inlet-1 50mm long. To simplify the computational problem, the distance from the symmetry plane to the clapboard was set to be three different dimensions, 105mm, 70mm and 25mm, respectively. Similarly, the height of the spreader was also set to be three different dimensions, 20mm, 10mm and 5mm. They would be explored by using numerical simulation at various boundary conditions, whereas the computational results were useful to understand how air fluid interacted with carbon fibers.

According to the simulation results, the spreader would be modified and spreader experiments would be undertaken to test the applicability of the 3-D mathematical model. First, the downstream pressures and velocities near the outlet were measured by precision pressure controller and digital micro-manometer, under various flow rates without carbon fiber tow, and the velocities would be compared with the calculated data to confirm the accuracy. Experiments of fiber spread were

executed at various fibers transporting rates and air flow rates. Photography techniques were used to record the processes of fibers spread. The photographs were taken from the top view. Five Nikon FM2 cameras were used and each was fitted with a 52mm lens. The single-frame photographs were taken with shutter speeds of 1/15 to 1/60 seconds, so that the images showed how fibers was spread and moved in the pneumatic spreader.

. Results and Discussion

A three-dimensional side-dump combustor chamber was performed to test the numerical program performance [40]. The 3-D combustor was referred to a full scale and real geometry, which has dual-inlets in opposition and the entered angle of the airflow between inlet and combustor is 60^0, as illustrated in Fig. 2-3(a). The numerical results indicated that there are four circulations caused by airflow entered the combustion chamber and bumped against each other; the flow field in the combustor was qualitatively agree with the experimental results, as shown in Fig. 2-3(b). Compared the velocity components with the numerical analysis by previous investigators, we also obtained a good agreement [40]. Therefore, the numerical program can be applied to the 3-D turbulent flow field analysis.

To study the geometry effect of the spreader, the simulation was conducted using height with three different dimensions, 20mm, 10mm and 5mm. Hence, there were three different cross-sectional areas, $500mm^2$ and $100mm^2$ at inlet-1 and inlet-2, for case 1, respectively, $250mm^2$ at inlet-1 and $50mm^2$ at inlet-2 for case 2, and $125mm^2$ at inlet-1 and $25mm^2$ at inlet-2 for case 3. The boundary conditions using pressure drop (0.275 psi) between upstream and downstream were given by Baucom et al.. It was found the pressure dropped abruptly as the cross-sectional area decreased, which caused a significant increment in air flow velocity at inlet-1 from 21.6 m/sec for case 1 up to 44 m/sec for case 3. The velocity increase is inversely proportional to the cross-sectional area, while the pressure drop is related to the square of the flow velocity. The pressure drop is also inversely proportional to the cross section of the

fiber flow outlet (inlet-1). Hence, the spreader model was set with 5mm in height.

The other parameter, the distance from symmetry plane to the clapboard, was also set with three dimensions 52.5mm, 37.5mm and 25mm, as shown in Fig. 2-4 and Fig. 2-5. The flow field for the distance 25mm was taken as an example shown in Fig. 2-6. The streamlines were plotted at the central plane (y = 25mm) of the mathematical model. There were three circulations in the spreader.

(1) The air was sucked into the spreader and then the air was accelerated due to sudden contraction at inlet-2. Therefore, the circulation zone was formed by fluid viscosity and drag.

(2) The air flow entered the inlet-1 and passed through the nine slots on the clapboard; thus, there were two circulation zones behind the clapboard.

However, the main interest of the present investigation was the flow field from the symmetry plane to the clapboard. While the distance increased from 25mm to 105mm, the circulation zone would increase at the inlet-2 and appear at the inlet-1; it makes fiber spread difficult. Since there was a slow velocity in the circulation zone, the fibers were hard to drag by air flow. In order to avoid the circulation zone, the distance from symmetry plane to the clapboard was set with 25mm. To understand the flow field under various boundary conditions, three cases with different pressure boundary conditions at the outlet surface were examined with the two parameters in the model. For the three cases, the pressures were 101100 Pa, 101200 Pa and 101250 Pa, respectively; however, the calculated flow fields were all very similar, so only the flow field for case 3 (101250 Pa) was shown in Fig. 2-6 and Fig. 2-7.

A velocity vector plot showed the main characteristics of the air flow. The

varieties of flow velocity appeared at inlet-1 and slots, since the cross-section area decreased. However, there was a stable flow at downstream around outlet. The velocity of air flow had an extremely small difference between inlet-1 and inlet-2. It is well known that $Q = \rho UA$, where Q is the flux; ρ is the fluid density; U is the fluid velocity, and A is the cross-sectional area of inlet. Furthermore, the flux at inlet-1 was 10 times larger than that at inlet-2, and the slots on the clapboard were close to the inlet-1; therefore, the main variations in air flow would occur at inlet-1 nearby, so we concentrated the discussion in the region from inlet-1 to slots.

A complete view of the pressure contour was seen in Fig. 2-8(a), which showed the low pressure distributed at the slots. A close-up view of the pressure contour in the vicinity of the inlet-1 was shown in Fig. 2-8(b). The detailed pressure distribution was calculated and had a slight difference about 30 Pa compared with the far field pressure of the spreader, but an evident difference was presented in case 1 (101100Pa). Therefore, if the simulation was in a low speed flow field, we could remove the outward block and take an ambient pressure boundary in the vicinity of the inlet-1 and inlet-2 to save the CPU time. In other words, the treatment of far field boundary conditions has good calculated results at high speed flow field. Fig. 2-9 showed that the calculated pressure distributions were at the inside and outside of inlet-1. It was clear that the pressure dropped abruptly due to a sudden contraction. There was a difference of about 20 Pa between the inside and outside of inlet-1. Additionally, a narrow low pressure zone (z=0.022m~0.025m) formed near the clapboard because the air flow passed through the separation location S; hence air flow separation occurred. Air could not enter this zone near the clapboard, so it was thin and there was no air

flow; thus, pressure dropped.

The distribution of the lateral velocity W was reduced with the distance Z approaching the symmetry plane. Inversely, the more air flowed into the inner location, the more velocity W increased. Above all, the most variation in the velocity W existed behind the slots. The calculated velocity W in the vicinity of inlet-1 was shown in Fig. 2-10. There was larger velocity at the outside of the inlet-1 near the clapboard, while the air was sucked into the spreader. It should be noted that the treatment of far field boundary could facilitate the calculation at the cross section of inlet-1. Generally, the calculation of the internal flow field set a uniform inflow at the inlet of a fluid; therefore, the numerical error could not be avoidable.

The W-velocity component at slot 1, slot 5 and slot 9 was calculated and presented in Fig. 2-11. Each curve represented the velocity variation from the symmetry plane perpendicular to the center of a slot. It was seen that air flowed toward the slots, yielding a slight change in velocity, but the magnitude of the velocity increased abruptly near the slots (Z = -0.02 m), since the cross-section area was suddenly contracted. The air entered the spreader through inlet-2 and turned toward slot 9; therefore, the W-velocity at slot 9 is larger than that at the other slots. The air flow was accelerated at the inside of the inlet-1 and inlet-2, and the large velocity U was near the symmetry plane. The U-velocity gradually decayed at the inner location, while the air flow turned toward the slots on the clapboard (-Z direction).

Figure2-12 presents the calculated U-velocity in the vicinity of the inlet-1. The U-velocity with an average velocity 0.6m/s at the outside of inlet-1 (x = -260 mm) was accelerated up to an averaged velocity 5.5m/s at the inside of inlet-1 (X = -248

mm). Moreover, as has been realized by previous discussion, the air flow could not enter the low pressure zone near the clapboard (Z = -0.22 m) due to the effect of separation flow. Hence little air flowed in this zone, such that the U-velocity decayed. The distribution of the U-velocity component from symmetry plane to the slots was shown in Fig. 2-13. The results indicated that there were smaller U-velocity components at the inner location due to the air flow changing direction. There was a negative U-velocity around slot 9; this was because airflow comes from inlet-2. In this investigation, as the V-velocity component was not found, it was found that the flow field was a two-dimensional flow in the spreader.

Figure 2-14 shows the speed variations in front of slot 1, slot 5 and slot 9. The speed was the resultant velocity of U- and W-velocity components. The results indicated that the main air flow come from inlet-1and there was similar magnitude of speed around each slot.
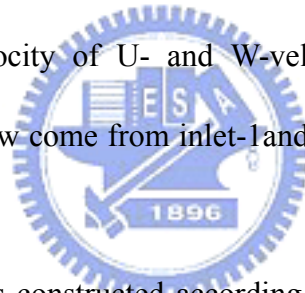
The physical model was constructed according to the designed parameters. To test the accuracy of the numerical model, a series of experimental measurements were made, and a comparison of the calculated velocity with the measurement is presented in the following figures. Fig. 2-15 showed a comparison between computation and measurement of the outlet velocity at the static pressure on the centerline of the outlet. It was found the computational data was in good agreement with the measured data. Similar trends were observed at the static pressure, 101200Pa, as shown in Fig. 2-16.

Theoretically speaking, the converged solution was calculated from upstream to downstream; moreover, the upstream computational results had the same order in numerical error as the downstream. The simulated and measured data were both

qualitatively and quantitatively similar; further, the 3-D computational results can be helpful for designing a pneumatic spreader. Although, considering no fiber addition, these results might not be precise enough to understanding interaction of fiber and air flow; the results gave us insight and led us to realize the 3-D flow field.

The air flux was related to the fluid velocity and pressure in the spreader, and was measured by the flow meter. They were measured and presented in Fig. 2-17(a) and 23(b). It was found that the mean mass flow rate was proportional to the mean static pressure and mean static pressure was also linearly increasing with mean fluid speed. Similarly, the computational results have the same the trend with the measured results. Therefore, the flow field can be qualitatively understood before the fiber spreading experiment is executed.

Figure 2-18 showed a fiber spreading experiment under V_F = 7 m/min and Q = 90 L/min, where V_F was the fiber transporting velocity and Q was the air mass flow rate. It was seen that the fibers were easily spread, and most fibers were dragged toward the clapboard and concentrated at the clapboard side. The reason was that the fluid velocity was fast.

While the conditions were set with V_F = 7 m/min and Q = 70 L/min, the fibers were spread in width about 20 mm at fiber exit. Fiber tow was spread by axial velocity; however, the axial velocity was not large enough to make fibers move to the location where the lateral W-velocity was larger. However, Baucom et al. argued that air entered through the tow exit and was drawn through the slots on the clapboard of the expansion section into a vacuum manifold. This cross-flow of air provided drag on the carbon fibers resulting in tow spread across the pneumatic spreader.

The fibers spread at the condition V_F = 7 m/min and Q = 80 L/min is shown as follows. Fig. 2-19(a) indicates the fiber tow was transported in the spreader. Initially, the fiber tow was spread out and fluffy at the fiber exit as shown in Fig. 2-19(b), because there was a maximum axial U-velocity at the exit (inlet-1) due to a sudden contraction and an acceleration of air flow. Sequentially, fibers were gradually spread out, and the partial spread of fiber extended to the inner of the spreader about the location of the fifth slot as shown in Fig. 2-19(c). Furthermore, the spread width at the inner location was slightly larger than that at fiber exit, since the air flow turned toward the slots. Comparing with Figure 2-2, it is seen that the air drag was gradually increased. Finally, fibers were dragged toward the clapboard and kept the width of the spreader as shown in Fig. 2-19(d). There were similar spread results at the other conditions, and the fiber spread procedure was all the same. However, Baucom et. al. reported that the 12k tow was spread to a 5.08 cm width at a tow rate , V_F = 3 m/min, and pressure drop was kept in P=0.275 psi.

In this study, we proposed an excellent performance and efficient application for spreading a fiber tow. Additionally, in a continuous fiber spreading procedure, there were three main steps recounted as follows:

(1) The fiber flow was firstly spread out at the fiber exit by the axial air flow.

(2) Fibers gradually moved toward lateral side, and the lateral W-velocity would influence the fiber movement.

(3) As the fibers moved closer to the clapboard, the W-velocity increased, and hence, the fibers were dragged toward the clapboard.

The proposed spreading procedure was more detailed and quite different from the one

Baucorn et al. described. Indeed, the 3-D computational results can be helpful for designing a pneumatic spreader. A pneumatic spreader must satisfy various requirements, such as stable flow field, avoiding circulation and vortex, and no abrupt velocity and pressure gradient variations in the spreader.

Although our simplified simulation without fiber tow may not be precise enough, the results give us detailed quantitative and quantitative observation to explore the 3-D flow field, i.e. velocity and pressure distribution. The comparison between the simulated and experimental result clearly shows that the numerical approach reported here can be used to study the pneumatic spreader.

. Conclusion

This is the first three-dimensional mathematical model of the fiber spreader and first time visualized by a photographic technique. The major results and conclusion from this work are summarized as follows:

1. The far field treatment at the boundary condition by a multi-block technique, extended the computational domain to far upstream, improved the calculated accuracy at the fiber exit (inlet-1), and it is more useful at large pressure drop conditions.

2. The turbulent k- model, incorporating a wall function ,is employed to study the fluid behavior of air flowing through the spreader. The circulation zone and separation flow can be simulated accurately.

3. The simulation results are in excellent agreement with the experimental measurements downstream, and the result can be used to analyze the flow field upstream. Therefore, the designed parameters are determined; the height of the spreader is 5 mm, and the distance from clapboard to symmetric plane is 25 mm.

4. The fiber tow was successfully spread out at various conditions, and the performance is better than prior study. The optimum and efficient condition in fiber spreading operation is V_F = 7 m/mim and Q = 80 L/min, and the operating pressure drop is 33 pa , which is smaller than Baucom et .al reported.

5. The fiber spreading procedures are first proposed, and they can help in understanding the spread process and provide the ability to test the design of the

pneumatic spreader.

6. The three-dimensional simulation is successfully combined with experiment for the application of carbon fiber tow spread, and this methodology can also used in other fiber spread processes.

. Refreences

[1] F. Delannay, L.Foryen, and A Deruyttere: Journal of Materials Science, 1987, vol. 22, pp. 1-16.

[2] R. V. Subramanian and A. Nyberg: J. Mater. Res., 1992, vol. 7, No. 3, pp. 677-688.

[3] Li-Min Zhou, Yiu-Wing-Mai and Caroline Baillie: Journal of Materials Science,1994, vol. 29, pp. 5541-5550.

[4] Sunil G., Warrier and Ray Y. Lin: Scripta Metallurgica et Materialia, 1993, vol. 29, pp. 1513-1518.

[5] Zhenhia Xia, Yaohe Zhou, Zhiying Mao, and Baolu Shang: Metallurgical Transcations B, 1992, vol. 23B, pp. 295-302.

[6] R. Asthana: Journal of Materials Science, 1998, vol. 33, pp. 1959-1980.

[7] G. Leonhardt, E. kieselstein, H. Podlesak, E. Than, and A. Hofman: Materials Science and Engineering, 1991, A135, pp. 157-160.

[8] Andreas Mortensen: Materials Science and Engineering, 1991, A135, pp. 1-11.

[9] J.K. Yu, H.L. Li, and B.L. Shang: Journal of Material Science, 1994, vol. 29, pp.2641-2647.

[10] D. Huda, M.A. El Baradie and M.S.J. Hashmi: Journal of Materials Processing Technology, 1993, vol. 37, pp. 529-541.

[11] Feng Wu and Jing Zhu: Composites Science and Technology, 1997, vol. 57, pp. 661-667.

[12] H. Nayeb Hashemi and J. Seyyedi: Metall. Trans. A, 1997, pp831

[13] M. F. Amateau: J. Compos. Mater., 1976, vol. 20 A, p.274

[14] R.T. Pepper and R. A. Penty: J. Composite Mater., 1974, vol. 8, p. 27-37.

[15] L. Xianguan and Z. Hanlin: Proc. 5th Int. Conf. on Composite Materials (ICCM-V, W. C. Harrigan, Jr. et al., eds., AIME, 1985, pp. 623-29)

[16] E. T. Thostenson, W. Z. Li., Z. Wang, Z. F. Ren, T. W. Chou: Journal of Applied Physics, 2002, vol. 1, no. 9, pp 6034-6037.

[17] Susan Abraham, B.C. Pai, K. G. Satyanarayana, and V. K. Vaidyan: Journal of Materials Science, 1999, vol. 25, pp. 2839-2845.

[18] S. Abraham, B.C. Pai, and K. G. Satyanaryana: Journal of Materials Science, 1992, vol. 27, pp. 3479-3486.

[19] H.M. Cheng, A. Kitahara, S. Akiyama, K. Kobayashi, and B. L. Zhou: Journal of Materials Science, 1992, vol. 27, pp. 3617-3623.

[20] Wang Yu-Qing, and Zhou Ben-Liam: Journal of Materials Processing Technology, 1998, vol. 73, pp. 78-81.

[21] Bobka, R.J., and L. P. Lowell:, Air Force Materials Laboratory, 1996, Part I, pp. 579-580.

[22] Clark, D., N.J. Wadsworth, and W. Watt: Proc. 2nd Carbon Fibre Conference, 1974, pp. 44.

[23] Haining Yang, Mingyuan Gu, Weiji Jiang and Guoding Zhang: Journal of Materials Science, 1996, vol. 31, pp.1903-1907.

[24] Clare G. Daniels, El Toro, and Calif: US Patent No. 3873389, 1975, March, 25.

[25] Paul E. McMahon, Tai-Shung Chung, and Lincoln Ying: US Patent No.4871491, 1989, Oct., 3.

[26] John N. Hall, Brookside Park, and Del: US Patent No. 3704485, 1972, Dec. 5.

[27] Robert M. Baucom and Johseph M. Marchello: Sampe Quarterly, 1990, July, pp. 14-19.

[28] Newell JA, Puzianowski AA. Development of a pneumatic spreading system for Kevlar-based SIC-precursor carbon fibre tows. High Perform Polym. 1999; 11: 197-203.

[29] Kawabe K, Tomoda S, Matsuo T. A pneumatic process for spreading reinforcing fiber tow. 42nd International SAMPE Symposium 1997; 65-76.

[30] J.F. Tompson: Numerical Grid Generation, Elsevier, New York, NY, 1982.

[31] CFX-F3D Version 4.1 User Manual, Harwell Laboratory, Oct., 1995.

[32] Valdimir D. Liseikin: Grid Generation Methods, Springer New York, 1999.

[33] Peter Bradshaw, Tuncer Cebeci and James H. Whitelaw: Engineering Calculation Methods for Turbulent Flow, Hsieh Chung, Taipei, 1981.

[34] E.B. Launder and B. D. Spalding: Mathematical Models of Turbulence, Academic Press, Londen 1972.

[35] Sturgess, G. J., Sayed, S. A. and Mcmanus, K. R.,:Int. J. Turbo and Jet Engines, 1986, 33, pp. 43-55.

[36] Eaton, J. K. and Johnston, J. P.,: AIAA J., 1981, vol. 19, no. 9, pp. 1093-1100.

[37] M. C. Rhie and L. W. Chow: AIAA journal, 1983, vol. 21, pp. 1525-1532.

[38] S.V. Patankar and B. D. Spalding: Int. J. Heat Mass Transfer, 1972, vol. 15, pp.1787-1792.

[39] C. A. J. Fletcher: Computational Techniques for Fluid Dymics, vol. 1, Fundamental and General Techniques 2nd Edi., Springer New York, 1991.

[40] Y. S. Hwang and T. M. Liu: Department of Power mechanical Engineering, National Tsing Hua University, Ph. D Thesis, 1989.

Table

c_1	c_2	c_μ	σ_k	σ_ε
1.44	1.92	0.09	1	2.9076
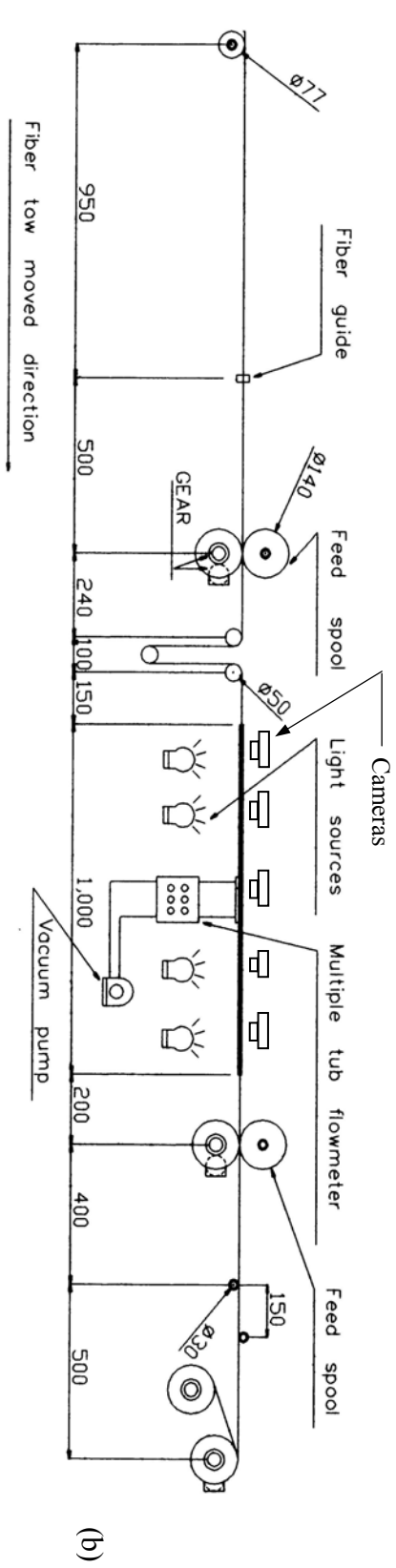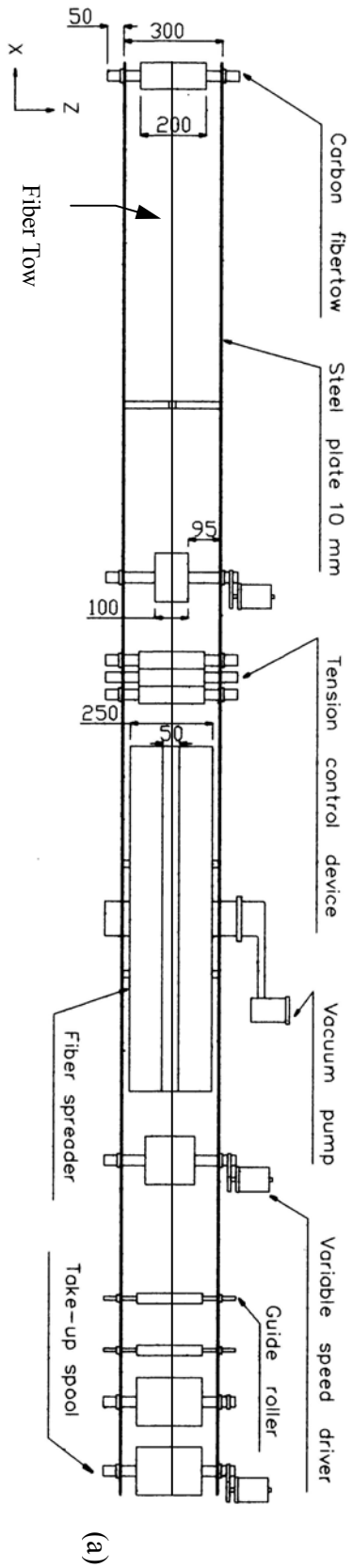
Fig. 2-1 A schematic diagram of the experimental setup for spreading carbon fiber tow (a) top view (b) side view.

SLOTS

INLET-1

OUTLET

50

195

25

110

1 2 3 4 5 6 7 8 9

250

CLAPBOARD

195

500

Origin

O

SYMMETRY
PLANE

2.5

125

INLET-2

Y(V)

Z(W)   X(U)

(a)

Unit: mm

Y (V)

Z (W)   X (U)

(b)

INLET-1

Extended Grids

SLOTS

CLAPBOARD

O

SYMMETRY PLANE — Origin
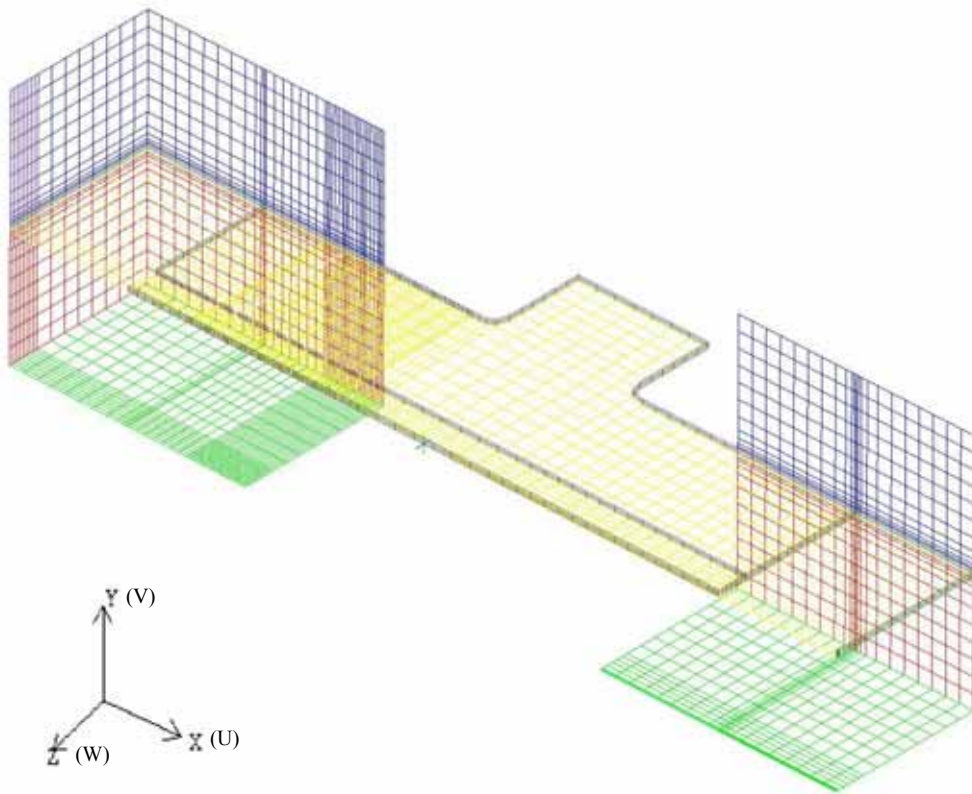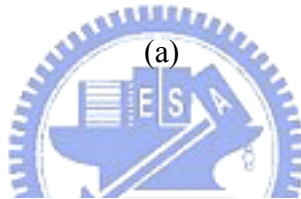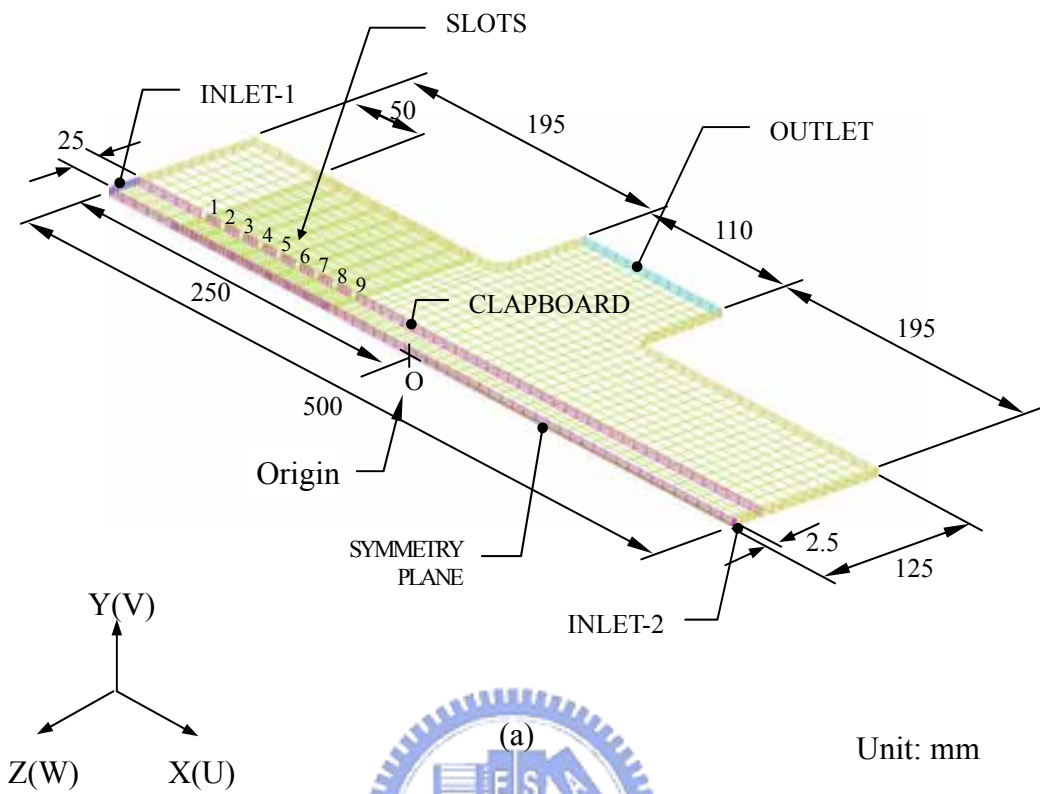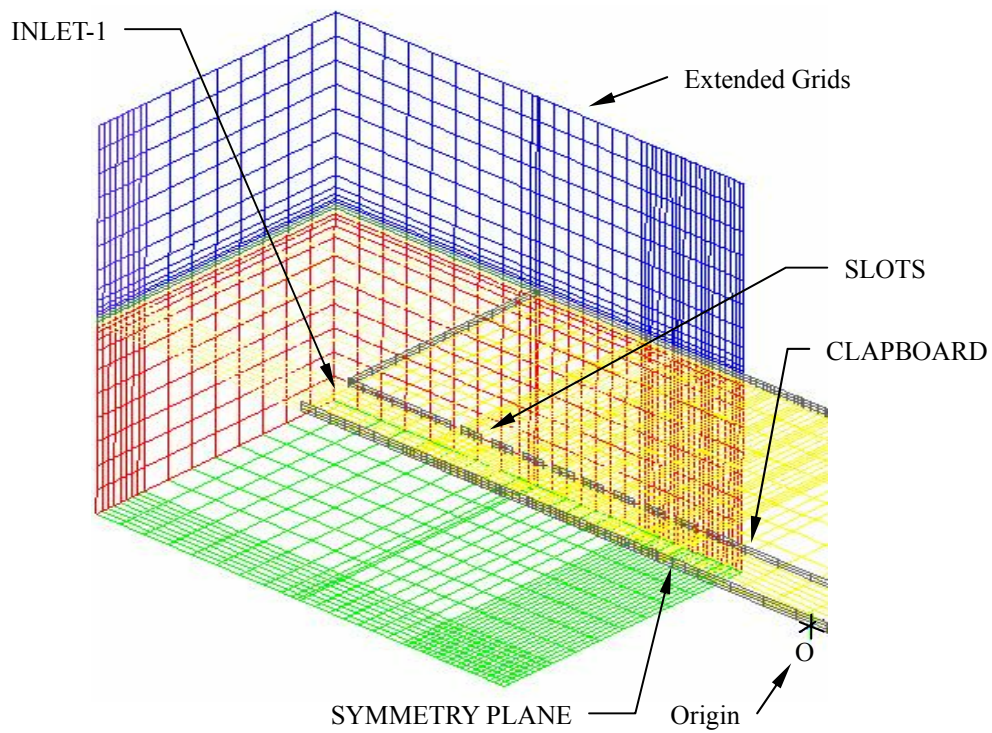
(c)

Fig. 2-2 (a) a three dimensional mathematical model of the pneumatic spreader in a isometric view, (b) a perspective of a far field treatment by multi-block technique in real space (U,V and W are the velocity components) and (c) an enlarged view.
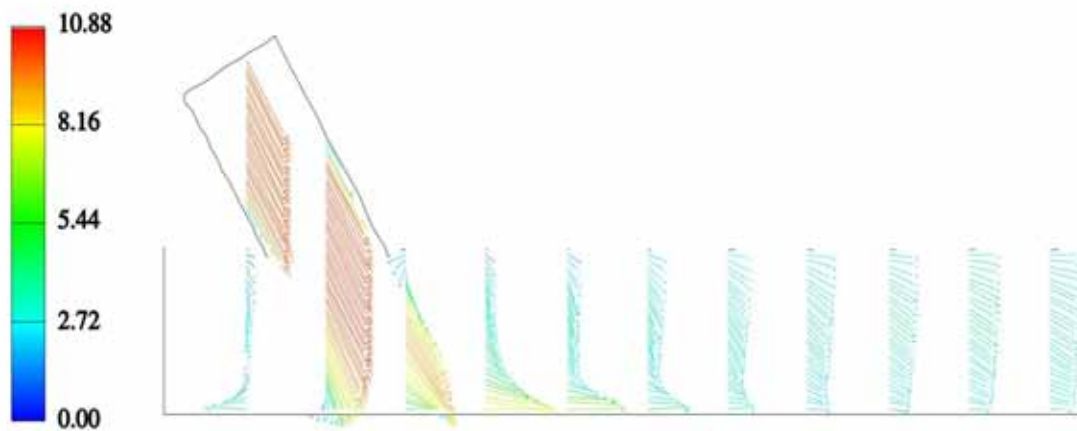
(a)
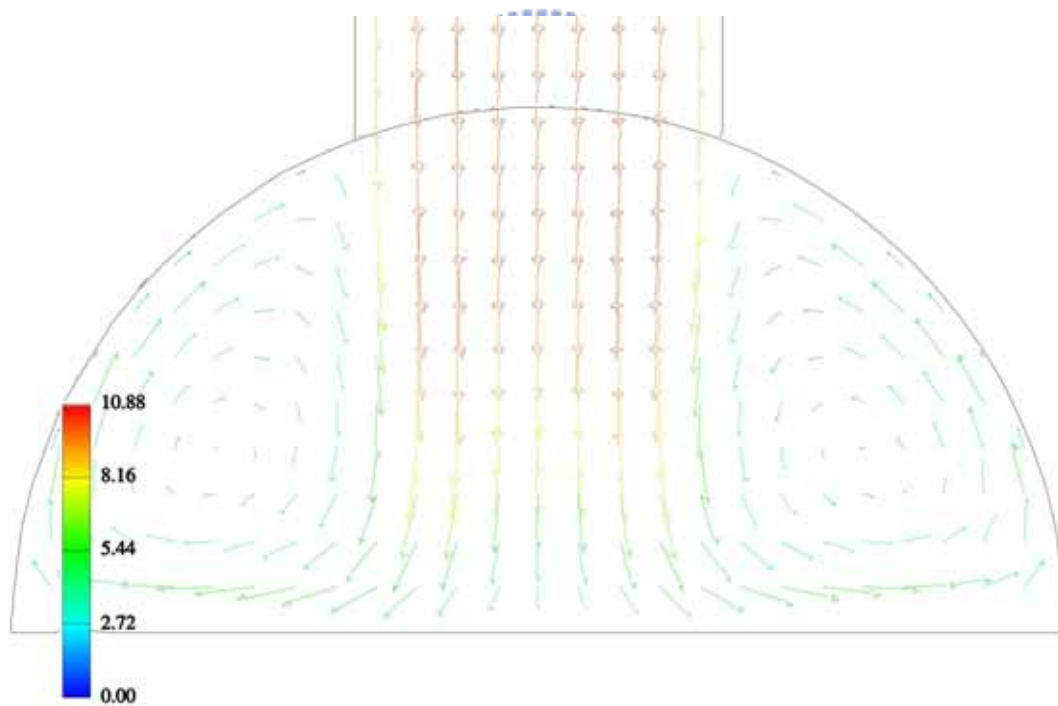
(b)

Fig. 2-3 A numerical simulation of 3-D flow field in a side-dump combustor (a) a complete view of velocity-vector at the central plane, (b) velocity-vector representation at the inlet of the cross-section.
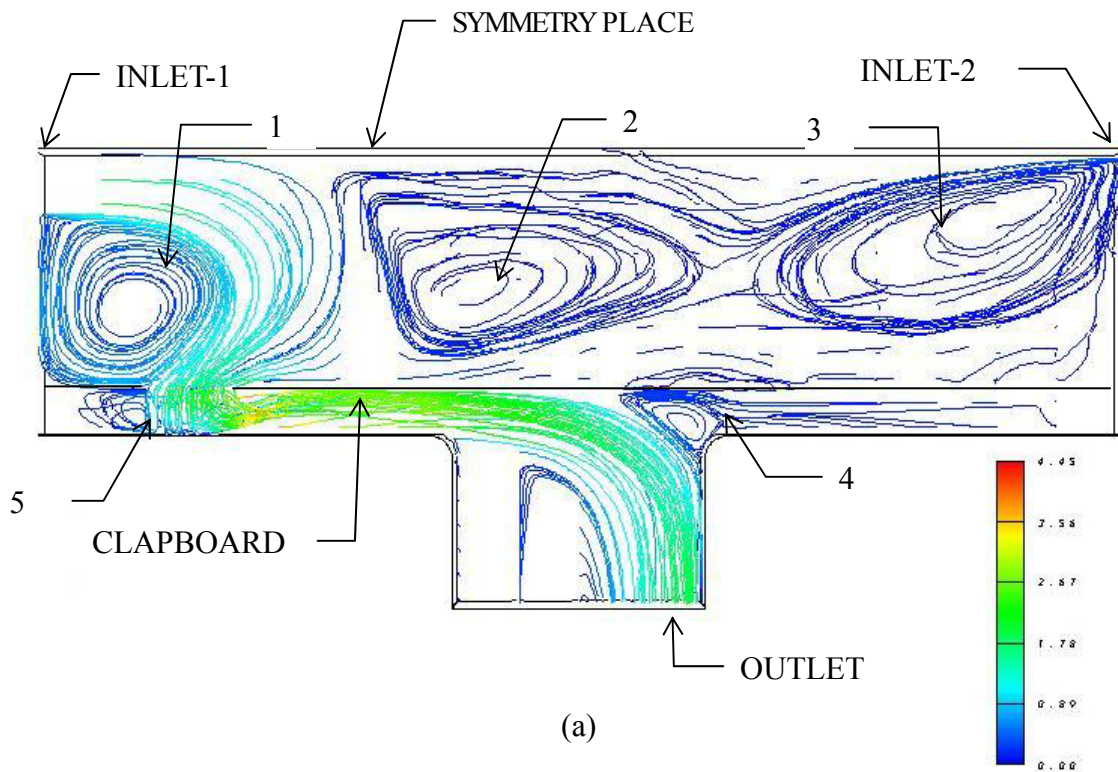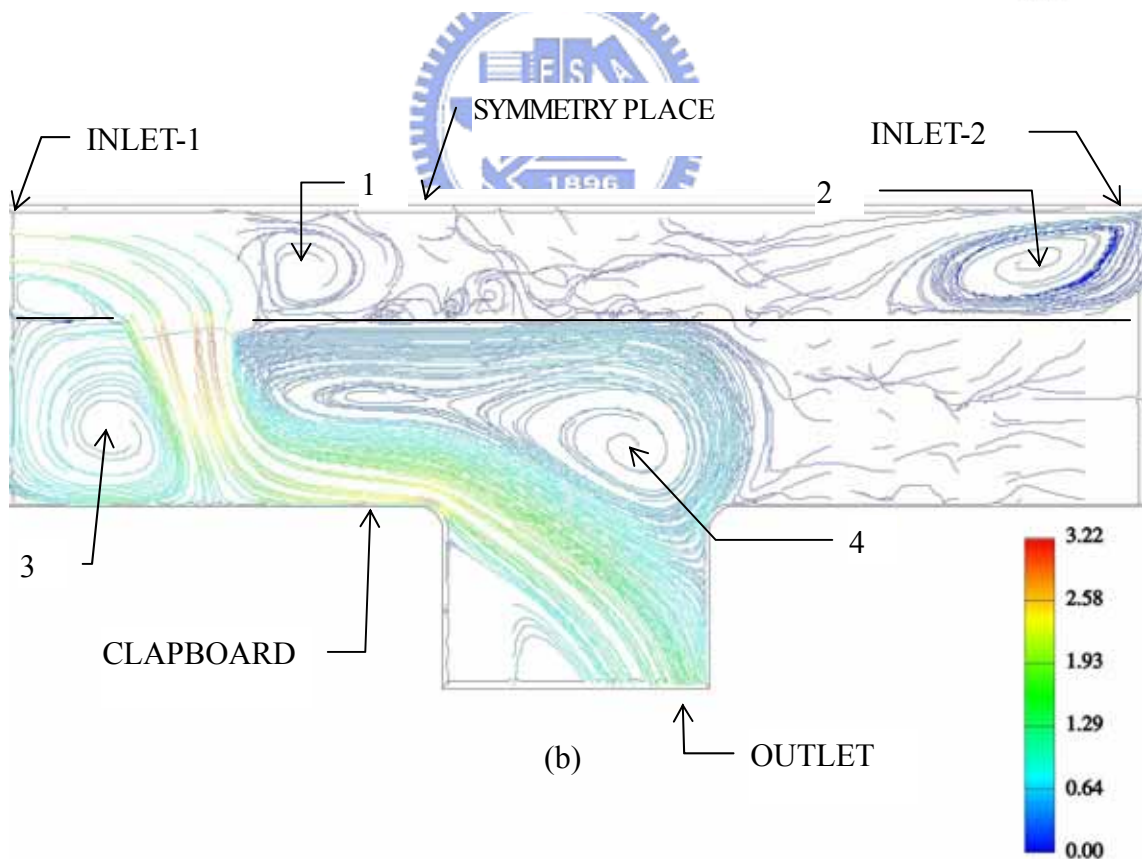
Fig. 2-4 A complete view of streamlines at the specification of the pneumatic spreader: (a) 52.5 mm and (b) 37.5 mm distance between clapboard and symmetry plane and 20 mm in high under the inlet velocity 2 m/sec.
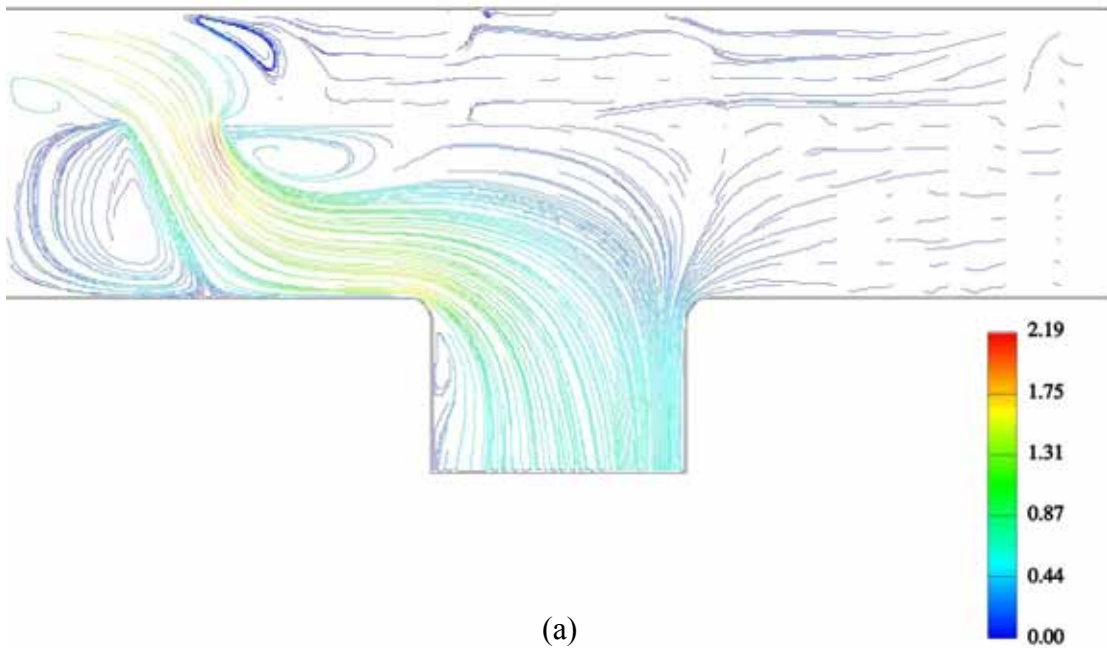
(a)
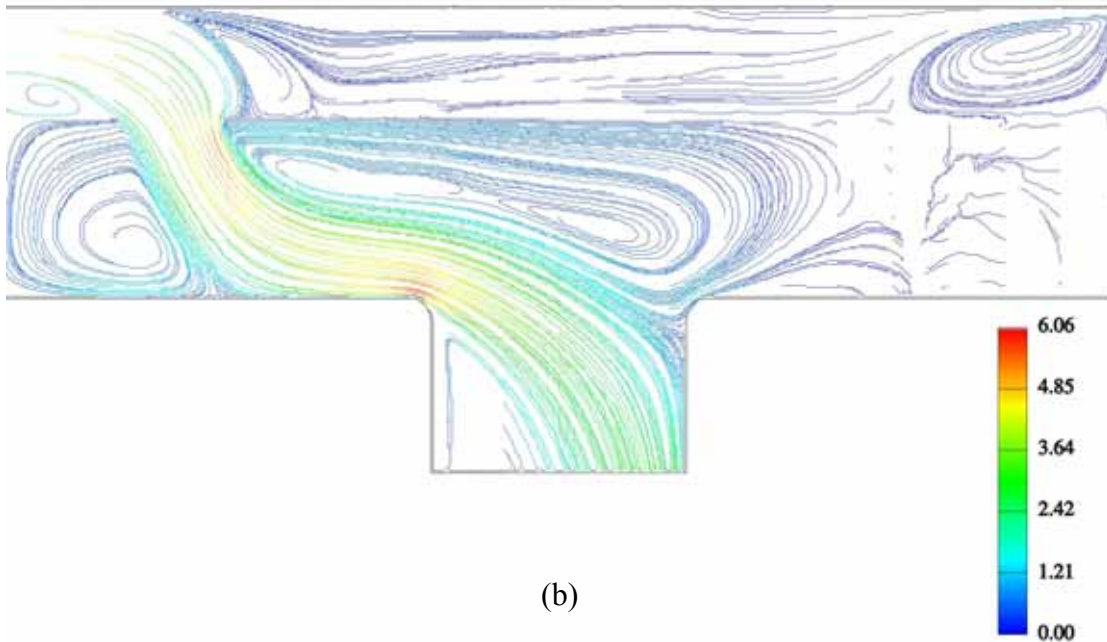
(b)

Fig. 2-5 A complete view of streamlines at the specification of the pneumatic spreader: 37.5 mm in distance between symmetry plane and clapboard and 5 mm in high under the pressure drop (a) 2 m/sec, (b) 5 m/sec.
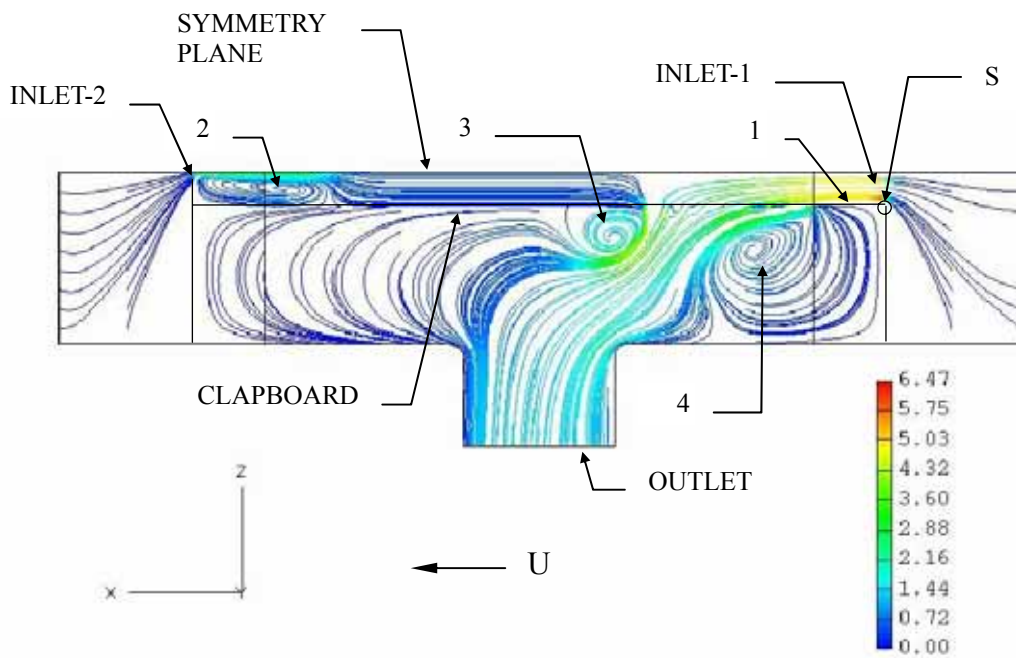
Fig. 2-6 A complete view of streamlines at the central plane (y=2.5 mm) under pressure drop 50 Pa between far field pressure boundary and outlet pressure boundary.
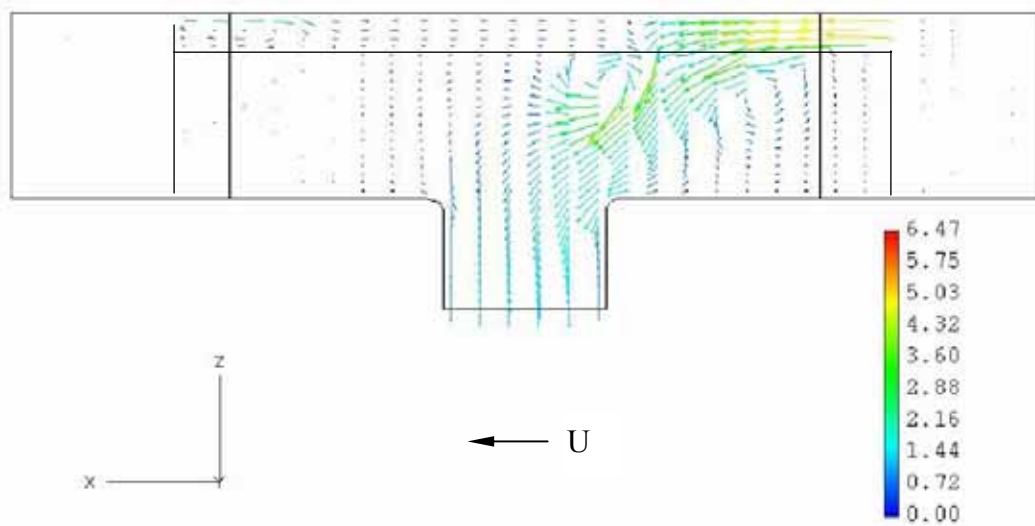
Fig. 2-7 Velocity-vector representation of the flow field
in Fig. 2-6.
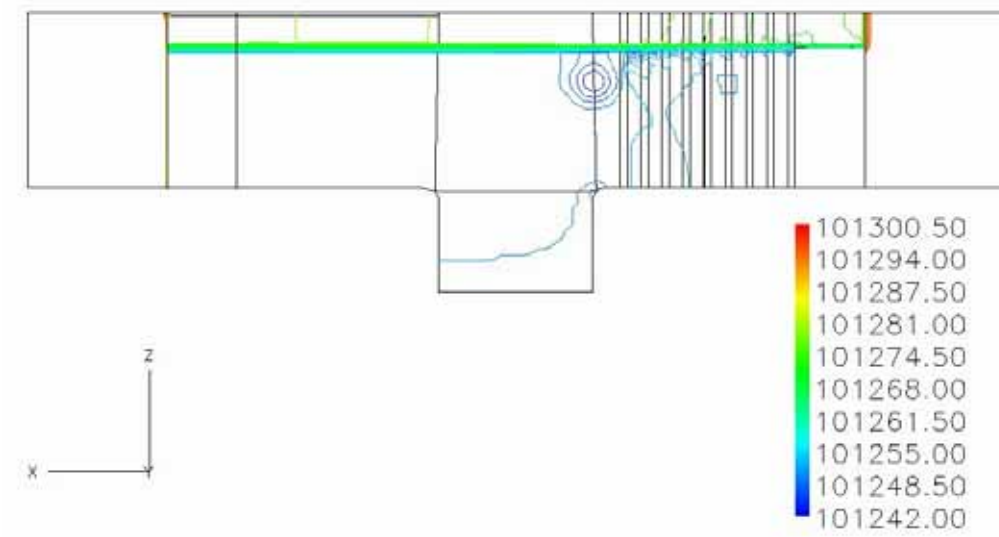
(a)
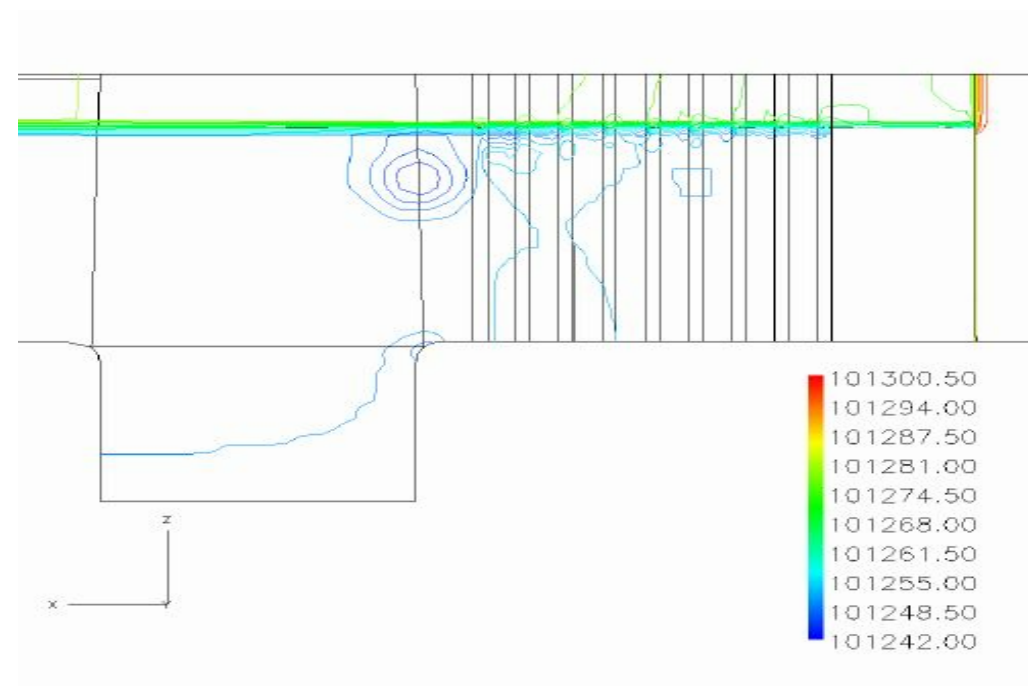
(b)

Fig. 2-8 Pressure contour under pressure drop 50 Pa (a)
a complete view, (b) a close-up view.
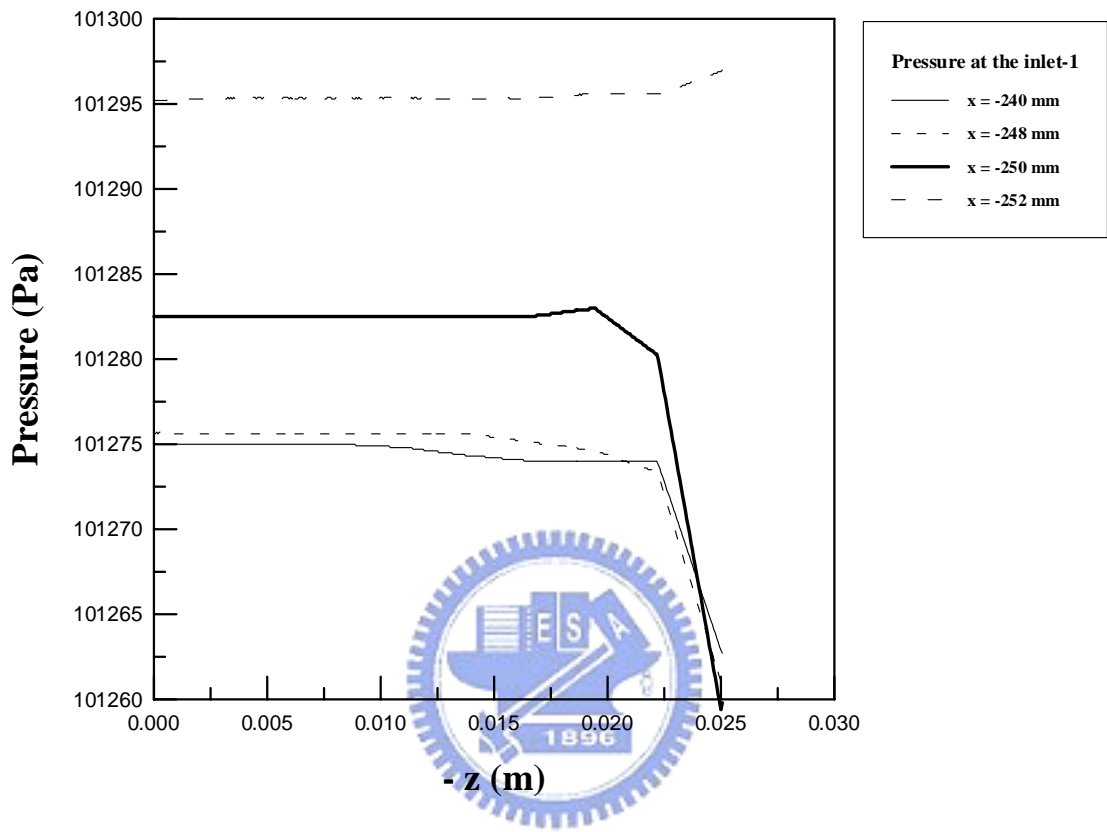
Fig. 2-9 Calculated pressure distributions at the inside and outside of the inlet-1(inside of the inlet-1:　　　　,
- - - - - ; inlet plane: ; outside ━━━ of the inlet-1:
).
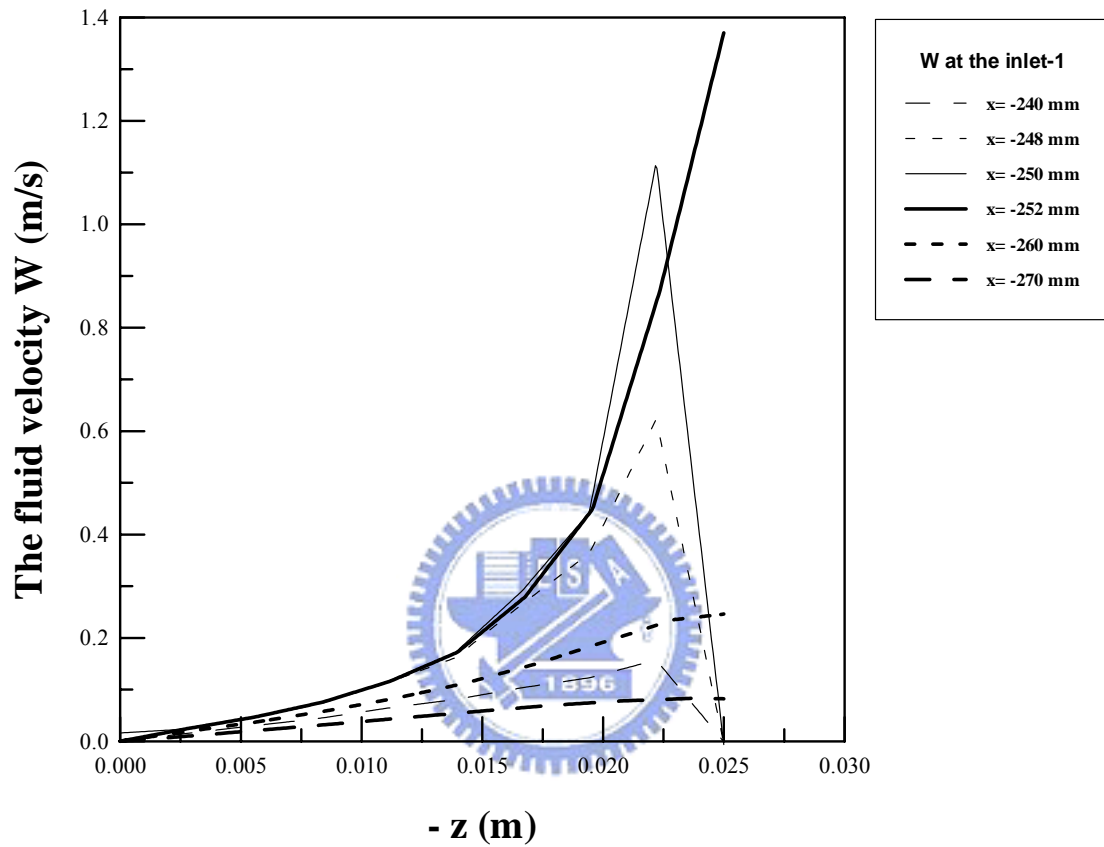
Fig. 2-10 Calculated W-velocity components from symmetry plane to the clapboard along –x direction in the vicinity of inlet-1 (inside of the inlet-1:   , - - - - - ; inlet plane ——— ;   outside of the inlet-1: ——— , - - - - - , ▬ ▬).
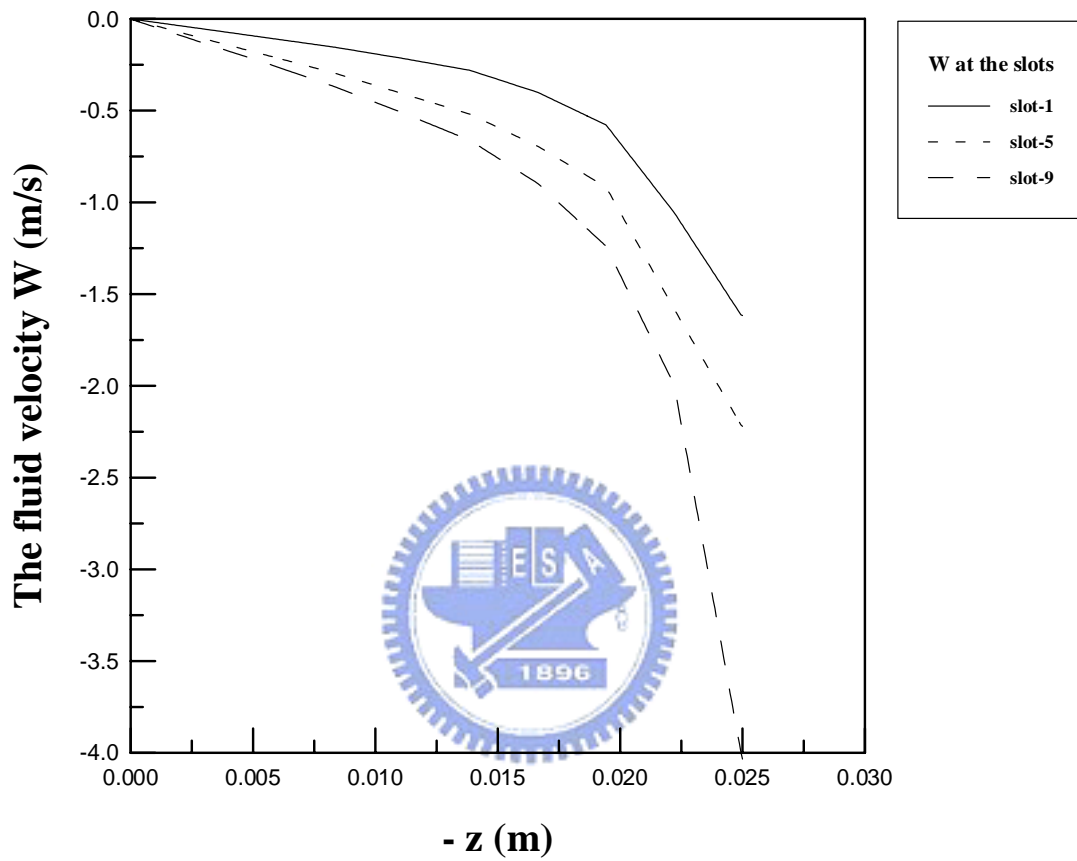
Fig. 2-11 Calculated W-velocity distributions from symmetry plane to the clapboard in front of slot 1, slot 5 and slot 9.
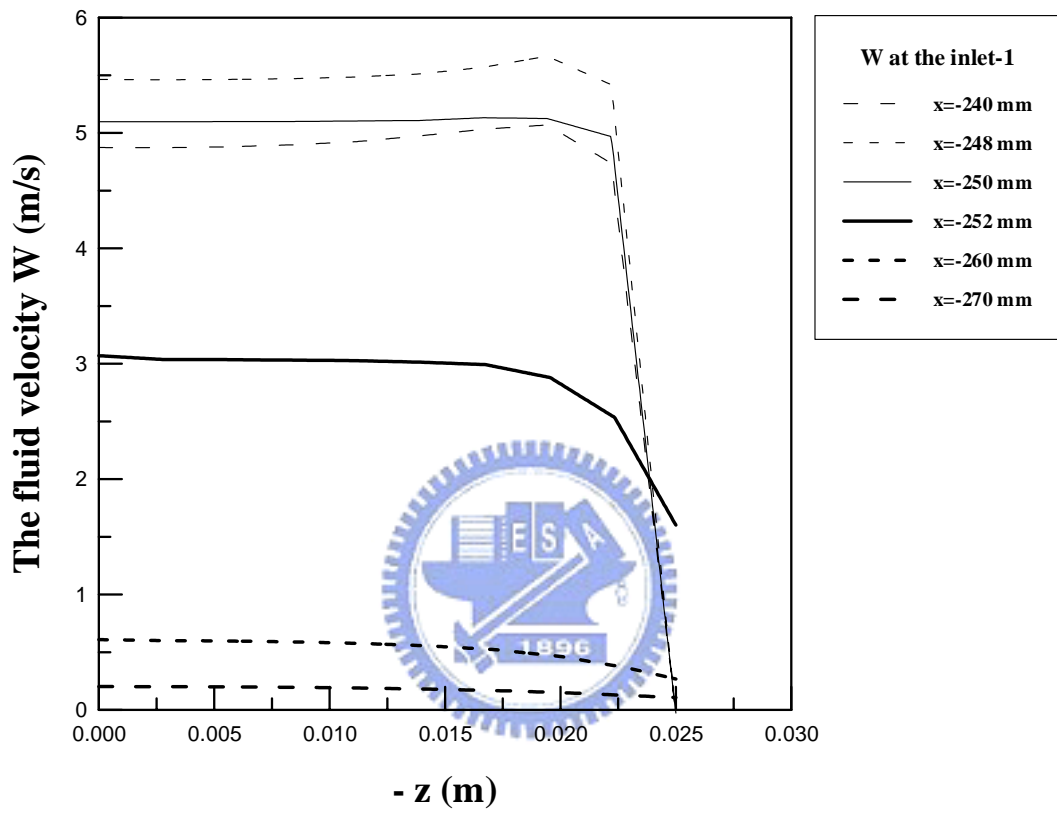
Fig. 2-12 Calculated U-velocity components from symmetry plane to the clapboard along –x direction in the vicinity of inlet-1.
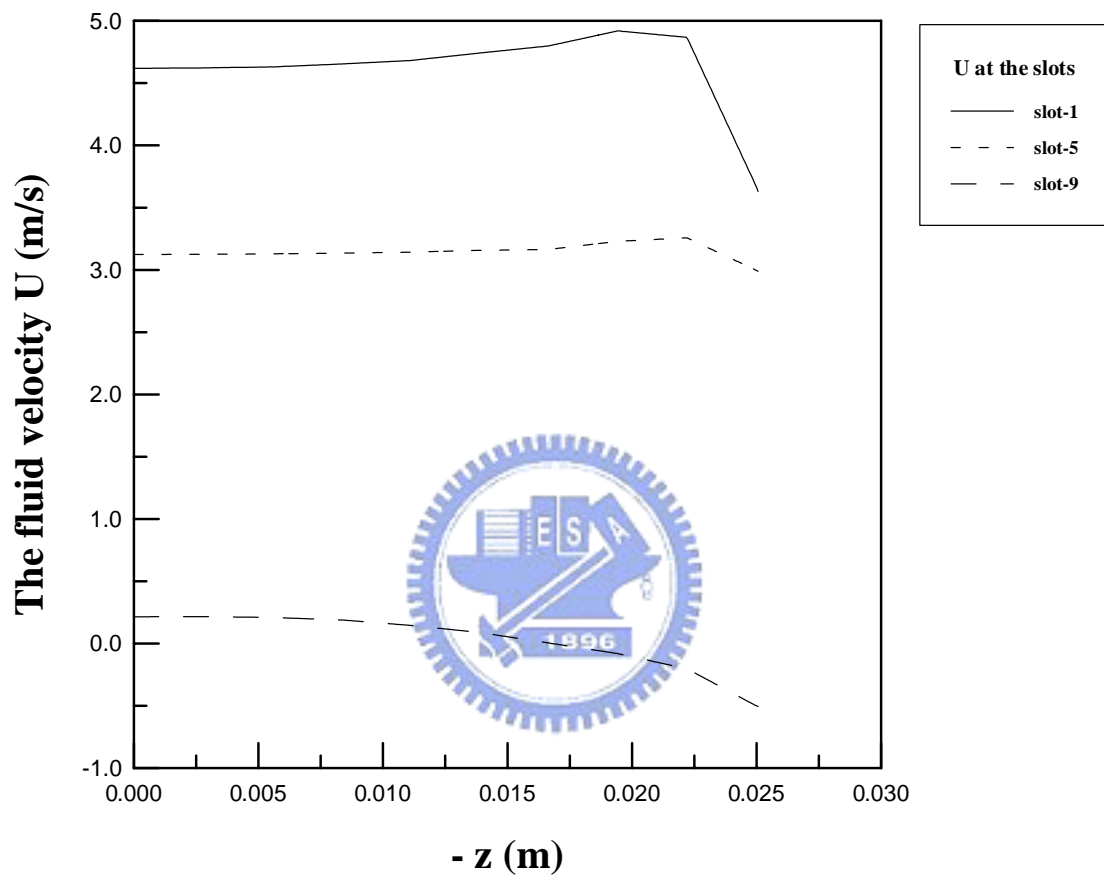
Fig. 2-13 Calculated U-velocity distributions from symmetry plane to the clapboard in front of slot 1, slot 5 and slot 9.
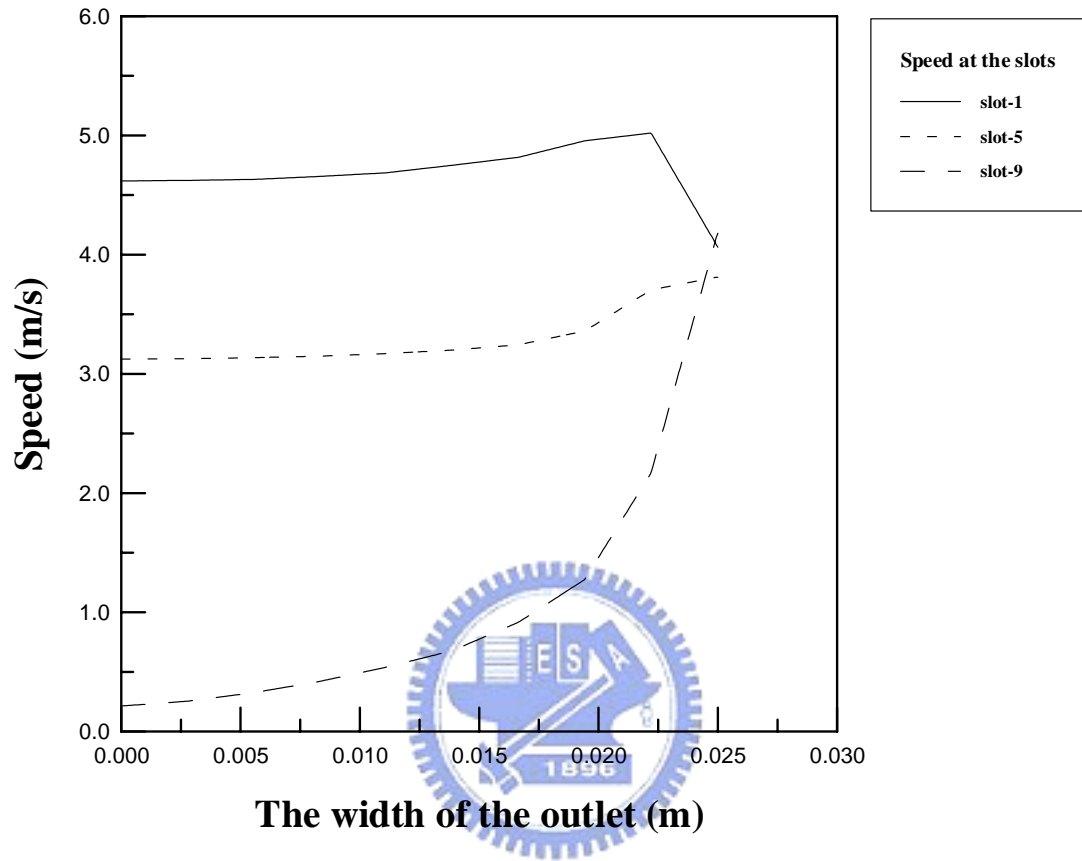
Fig. 2-14 Calculated speed distributions from symmetry plane to the clapboard in front of slot 1, slot 5 and slot 9.
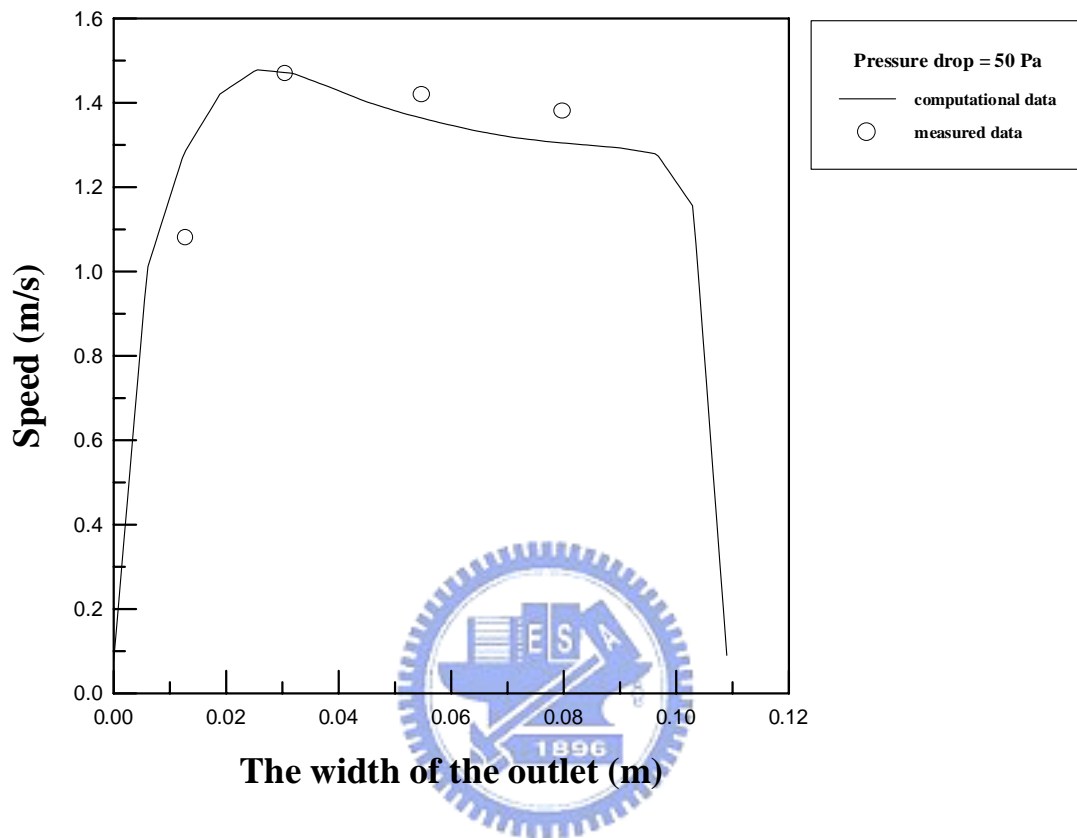
Fig. 2-15 Comparison of computational and measured
speed at outlet under pressure drop 50 Pa.
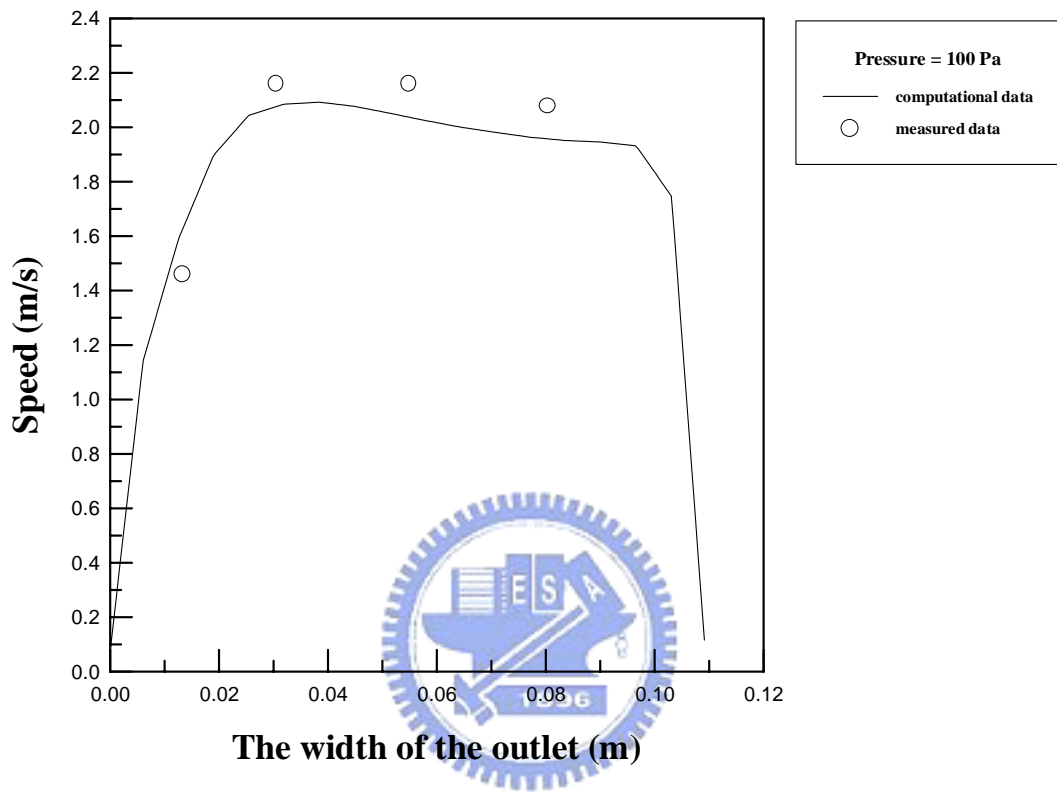
Fig. 2-16 Comparison of computational and measured speed at outlet pressure drop 100 Pa.

70
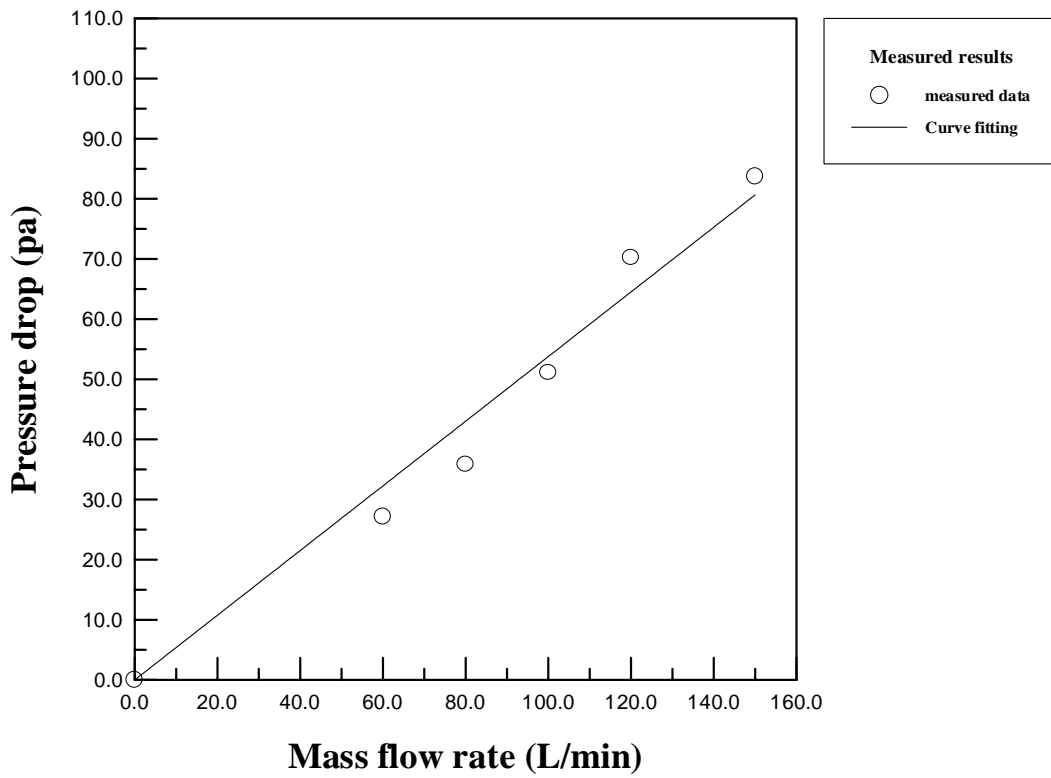
(a)
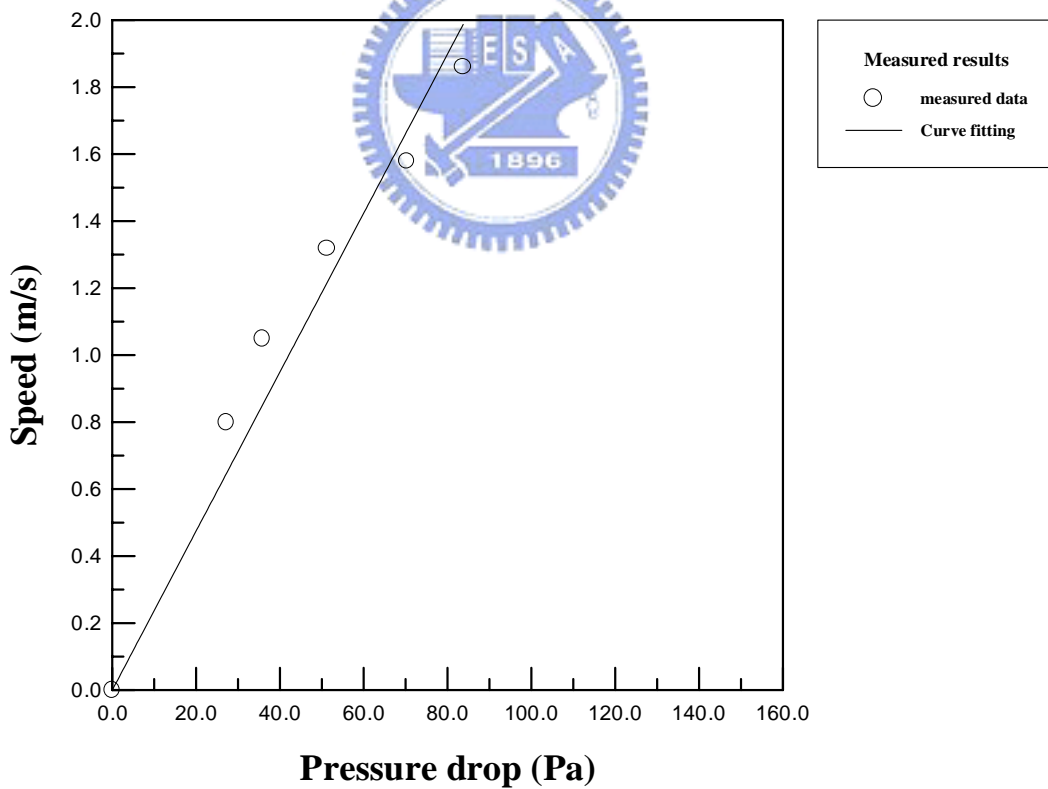
(b)

Fig. 2-17 (a) The relations of the experimentally measured mean mass flow rates and pressure drops at outlet, (b) the relations of the experimentally measured pressure drops and speeds at outlets.
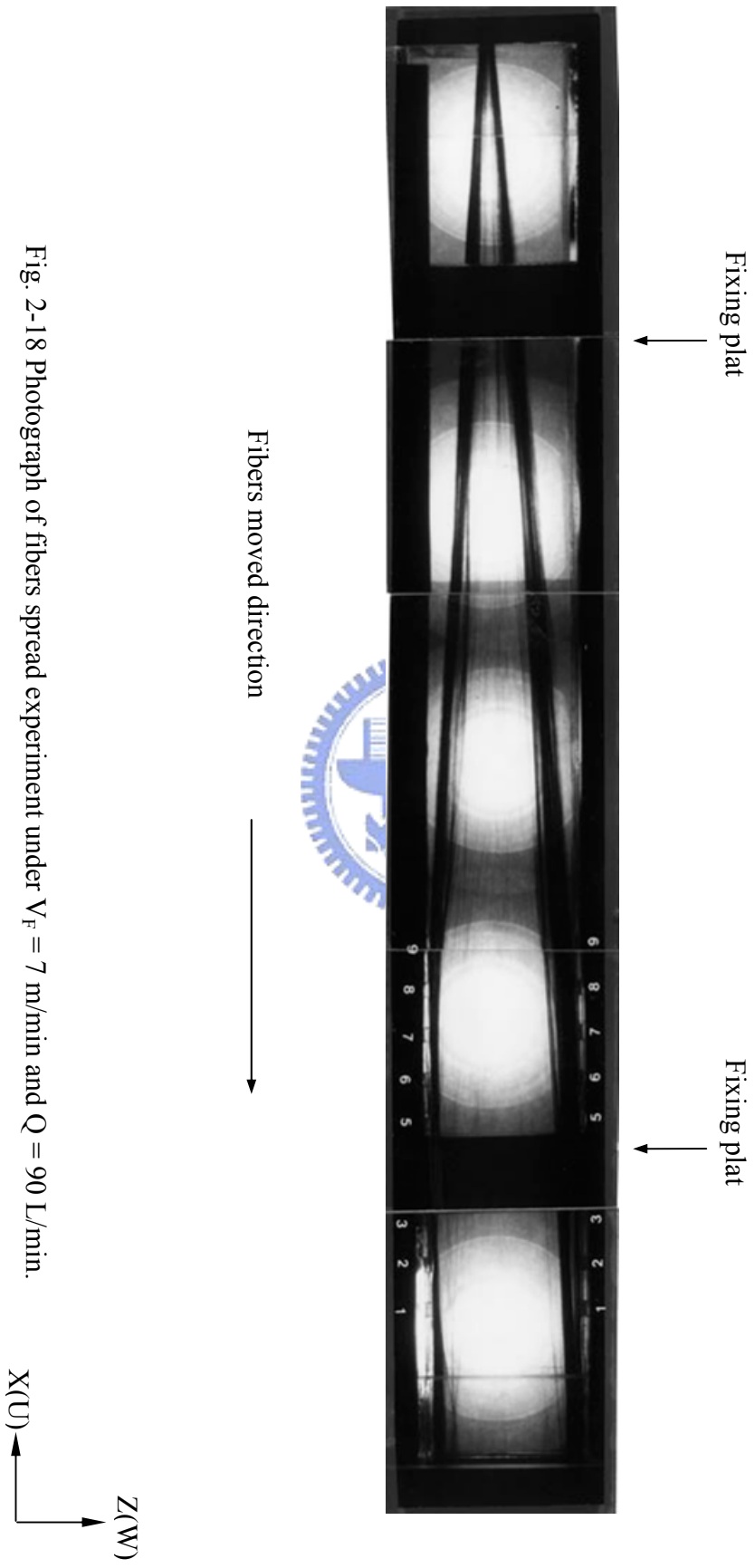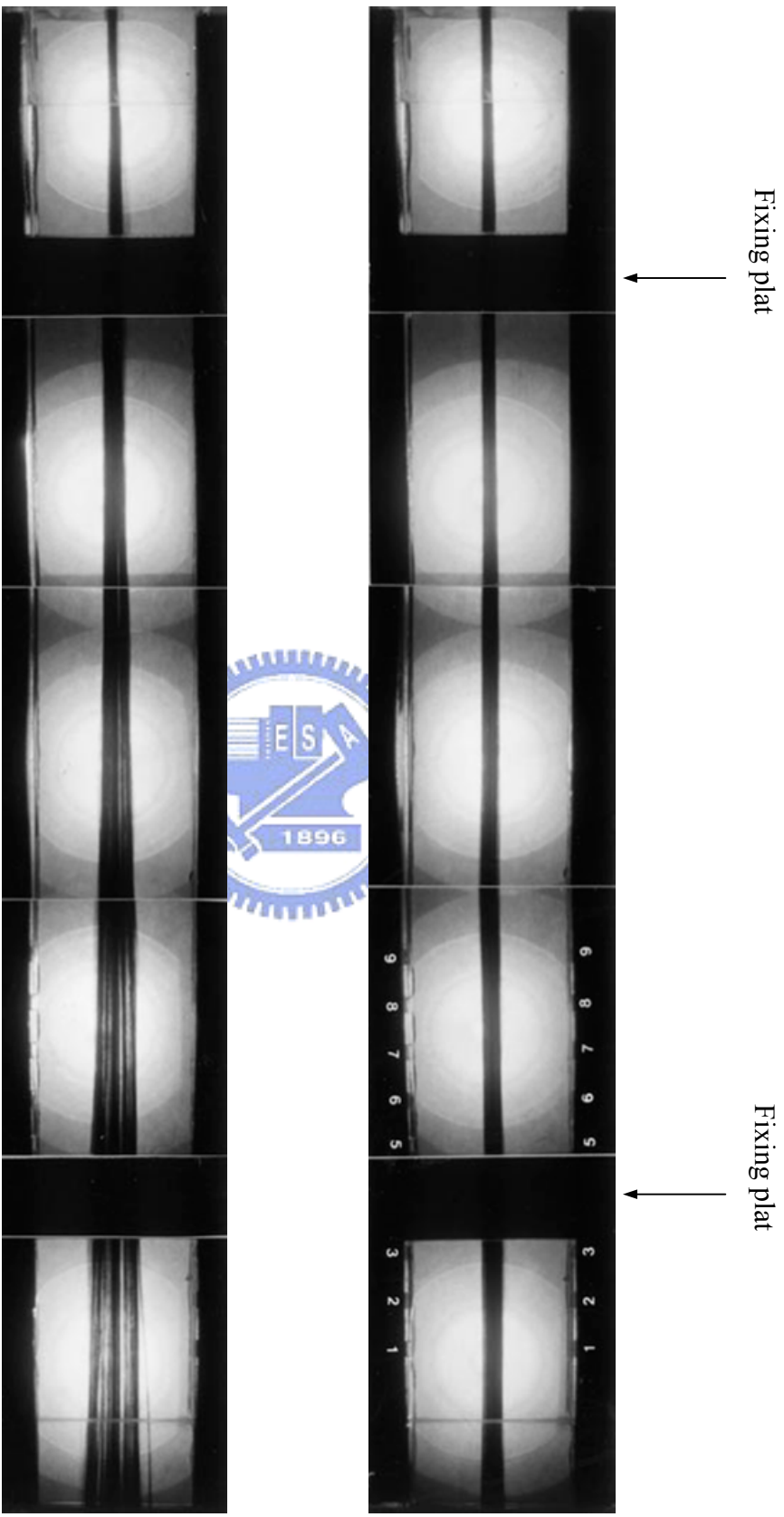
Fig. 2-18 Photograph of fibers spread experiment under $V_F = 7$ m/min and $Q = 90$ L/min.

72

Fixing plat

Fixing plat

Fibers moved direction
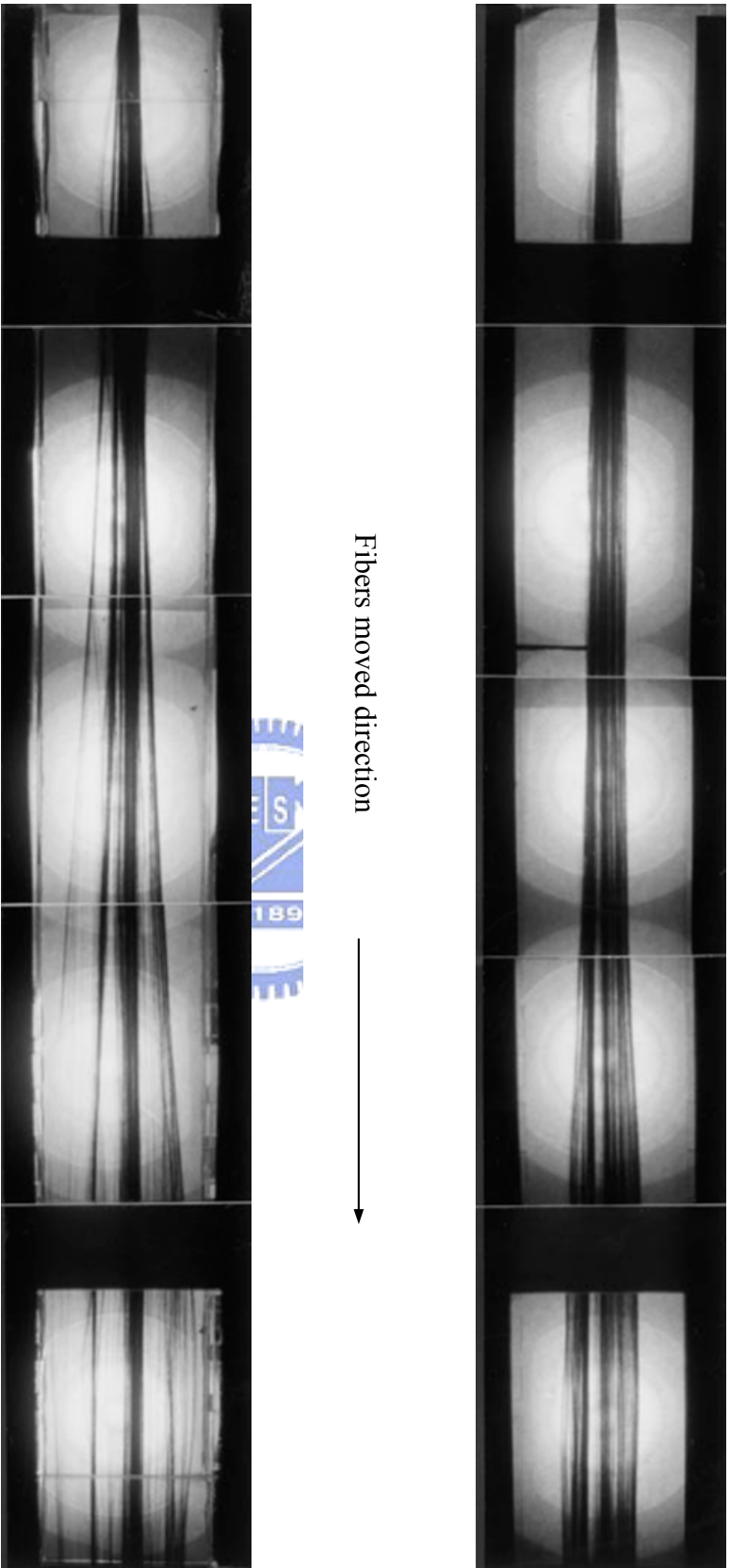
X(U)

Z(W)

(a)

(b)

73

Fig. 2-19 Photographs of fibers spread experiment under $V_F = 7$ m/min and $Q = 80$ L/min. (a) initial state (b) fibers spread to lateral side, (c) more fibers moved to lateral side, (d) final state.

Fibers moved direction

X(U)

Z(W)

(c)

(d)